Nonlinear material identification of heterogeneous isogeometric Kirchhoff-Love shells

Bartosz Borzeszkowski[a], Izabela Lubowiecka[a], Roger A. Sauer[a,b,c,*]

[a] *Gdańsk University of Technology, Faculty of Civil and Environmental Engineering, ul. Narutowicza 11/12, 80-233 Gdańsk, Poland*

[b] *Aachen Institute for Advanced Study in Computational Engineering Science (AICES), RWTH Aachen University, Templergraben 55, 52056 Aachen, Germany*

[c] *Department of Mechanical Engineering, Indian Institute of Technology, Kanpur, UP 208016, India*

Published[†] in *Comput. Methods Appl. Mech. Eng.*, DOI: 10.1016/j.cma.2021.114442
Submitted on 11 August 2021; Revised on 11 November 2021; Accepted on 5 December 2021

Abstract: This work presents a Finite Element Model Updating inverse methodology for reconstructing heterogeneous material distributions based on an efficient isogeometric shell formulation. It uses nonlinear hyperelastic material models suitable for describing incompressible material behavior as well as initially curved shells. The material distribution is discretized by bilinear elements such that the nodal values are the design variables to be identified. Independent FE analysis and material discretization, as well as flexible incorporation of experimental data, offer high robustness and control. Three elementary test cases and one application example, which exhibit large deformations and different challenges, are considered: uniaxial tension, pure bending, sheet inflation, and abdominal wall pressurization. Experiment-like results are generated from high-resolution simulations with the subsequent addition of up to 4% noise. Local optimization based on the trust-region approach is used. The results show that with a sufficient number of experimental measurements, design variables and analysis elements, the algorithm is capable to reconstruct material distributions with high precision even in the presence of large noise. The proposed formulation is very general, facilitating its extension to other material models, optimization algorithms and meshing approaches. Adapted material discretizations allow for an efficient and accurate reconstruction of material discontinuities by avoiding overfitting due to superfluous design variables. For increased computational efficiency, the analytical sensitivities and Jacobians are provided.

Keywords: Finite Element Model Updating method, material identification, heterogeneous materials, inverse problems, isogeometric analysis, nonlinear Kirchhoff-Love shells.

List of important symbols

$\boldsymbol{a}_\alpha$	covariant tangent vectors of surface $\mathcal{S}$ at point $\boldsymbol{x}$; $\alpha = 1,2$
$\boldsymbol{A}_\alpha$	covariant tangent vectors of surface $\mathcal{S}_0$ at point $\boldsymbol{X}$; $\alpha = 1,2$
$\boldsymbol{a}^\alpha$	contravariant tangent vectors of surface $\mathcal{S}$ at point $\boldsymbol{x}$; $\alpha = 1,2$
$\boldsymbol{A}^\alpha$	contravariant tangent vectors of surface $\mathcal{S}_0$ at point $\boldsymbol{X}$; $\alpha = 1,2$
$\boldsymbol{a}_{\alpha,\beta}$	parametric derivative of $\boldsymbol{a}_\alpha$ w.r.t. ξ^β
$a_{\alpha\beta}$	covariant metric components of surface $\mathcal{S}$ at point $\boldsymbol{x}$
$A_{\alpha\beta}$	covariant metric components of surface $\mathcal{S}_0$ at point $\boldsymbol{X}$
$\mathbf{B}^e$	matrix of the coefficients of the Bernstein polynomials for element Ω^e
$b_{\alpha\beta}$	covariant curvature tensor components of surface $\mathcal{S}$ at point $\boldsymbol{x}$
$B_{\alpha\beta}$	covariant curvature tensor components of surface $\mathcal{S}_0$ at point $\boldsymbol{X}$
c	bending stiffness

---

[*] corresponding author, email: sauer@aices.rwth-aachen.de

[†] This pdf is the personal version of an article whose journal version is available at https://sciencedirect.com

$\mathbf{C}^e_\alpha$	Bézier extraction operator for element Ω^e in direction ξ_α
$\Gamma^\gamma_{\alpha\beta}$	Christoffel symbols of the second kind of surface $\mathcal{S}$
$\mathrm{d}a$	differential area element on $\mathcal{S}$
$\mathrm{d}A$	differential area element on $\mathcal{S}_0$
$\delta\ldots$	variation of ...
d	number of displacement dofs per analysis node (= 3 in 3D)
$\bar{d}$	number of material dofs per material node (= 1 in Secs. 5.1 & 5.2, otherwise = 2)
δ_{max}	maximum of the relative error between reference and estimated parameters
δ_{ave}	average of the relative error between reference and estimated parameters
e	index numbering of elements
E	Young's modulus
$\varepsilon_{\alpha\beta}$	covariant components of the membrane strain tensor
e^α	offset between Ω^e_0 and $\bar{\Omega}^e_0$ coordinate centers
$\ldots^{\mathrm{exp}}$	corresponding quantity of the experimental grid; e.g. $\boldsymbol{x}^{\mathrm{exp}}_I$
f	objective function
$\boldsymbol{f}$	'body' force acting on $\mathcal{S}$
$\boldsymbol{F}$	surface deformation gradient
$\boldsymbol{f}_0$	constant surface force (due to dead loading)
$\mathbf{f}^e_\bullet$	finite element force vector of element Ω^e
$\mathbf{g}$	gradient of the objective function f
G	expression for the weak form
G^e	contribution to G from finite element Ω^e
G_{ext}	external virtual work
G_{int}	internal virtual work
$\ldots^h$	... approximated by finite elements
$\mathbf{H}$	Hessian of the objective function f
I	index numbering of finite and material element nodes, and experimental points
J	area change between $\mathcal{S}_0$ and $\mathcal{S}$
$\mathbf{J}$	Jacobian of the residual $\bar{\mathbf{U}}_{\mathrm{r}}$
$\kappa_{\alpha\beta}$	covariant components of the relative curvature tensor
$\mathbf{K}$	global finite element tangent matrix
$\mathbf{k}^e$	elemental finite element tangent matrix associated with $\mathbf{f}^e$
Λ	2D Lamé parameter
$\tilde{\Lambda}$	3D Lamé parameter
m_τ, m_ν	bending moment components acting at $\boldsymbol{x} \in \partial\mathcal{S}$
$M^{\alpha\beta}$	contravariant bending moment components
$M^{\alpha\beta}_0$	$= JM^{\alpha\beta}$
μ	2D surface shear modulus
$\tilde{\mu}$	3D shear modulus
$\boldsymbol{n}$	surface normal of $\mathcal{S}$ at $\boldsymbol{x}$
$\boldsymbol{N}$	surface normal of $\mathcal{S}_0$ at $\boldsymbol{X}$
$\mathcal{N}$	trust region
$\mathbf{N}$	array of the shape functions for element Ω^e
$\bar{\mathbf{N}}$	array of the shape functions for element $\bar{\Omega}^e$
N_I	displacement shape function of finite element node I
$\bar{N}_I$	shape function of material element node I
n_{el}	total number of FE used to discretize $\mathcal{S}$
n_{ll}	number of load levels considered in the experiment
$\bar{n}_{\mathrm{el}}$	total number of material elements used to discretize q
n_{exp}	number of sampled experimental points for all n_{ll} load levels
n_{no}	number of FE analysis nodes

$\bar{n}_{\text{no}}$	number of material nodes
n_e	number of nodes of Ω^e
$\bar{n}_e$	number of nodes of $\bar{\Omega}^e$
n_{var}	number of design variables
ν	Poisson's ratio
$\boldsymbol{\nu}$	normal vector on boundary $\partial\mathcal{S}$
p	external pressure normal to $\mathcal{S}$
$\mathcal{P}$	parametric domain spanned by ξ^1 and ξ^2
q	material parameter field
$\mathbf{q}$	stacked array of all nodal $\mathbf{q}^e$ in the system
$\mathbf{q}^e$	stacked array of all nodal q_I of material element $\bar{\Omega}^e$
q_I	material parameter value at material node I
$\mathbf{q}_{\text{opt}}$	solution of the inverse problem
$\mathbf{q}_0$	initial estimate for the optimization
$\mathbf{R}$	vector of reaction forces
$\mathbf{S}$	sensitivity matrix
$\mathcal{S}$	current configuration of the surface
$\mathcal{S}_0$	initial configuration of the surface
$\mathbf{s}_k$	trial step at inverse iteration k
$\boldsymbol{\sigma}$	surface Cauchy stress tensor of $\mathcal{S}$ at point $\boldsymbol{x}$
$\sigma^{\alpha\beta}$	contravariant in-plane stress components
$\boldsymbol{t}^\alpha$	traction vector acting on the surface $\perp \boldsymbol{a}^\alpha$
$\boldsymbol{t}$	effective traction acting on boundary $\partial\mathcal{S}$
T	reference thickness of $\mathcal{S}$
$\boldsymbol{\tau}$	surface Kirchhoff stress tensor of $\mathcal{S}$ at $\boldsymbol{x}$
$\tau^{\alpha\beta}$	$= J\sigma^{\alpha\beta}$ Kirchhoff membrane stress components
$\boldsymbol{\varphi}$	deformation map of surface $\mathcal{S}$
$\boldsymbol{u}$	displacement field of $\mathcal{S}$ at $\boldsymbol{x}$
$\bar{\boldsymbol{u}}$	prescribed boundary displacements on Dirichlet boundary $\partial_u\mathcal{S}$
$\mathbf{u}_\bullet^\bullet$	discrete displacements; $\bullet$ takes the same options as in $\mathbf{x}_\bullet^\bullet$
$\mathbf{U}_{\text{exp}}$	stacked vector of n_{exp} experimentally measured displacements $\boldsymbol{u}_I$ at surface point $\boldsymbol{x}_I$
$\mathbf{U}_{\text{FE}}$	vector of FE surface displacements $\boldsymbol{u}^h$ interpolated at all n_{exp} experimental points $\boldsymbol{x}_I^{\text{exp}}$
$\bar{\mathbf{U}}_{\text{r}}$	residual vector
W	2D hyperelastic stored surface energy density
$\mathcal{V}$	space of admissible functions
$\boldsymbol{x}$	current position on surface $\mathcal{S}$
$\boldsymbol{X}$	initial position on surface $\mathcal{S}_0$
$\mathbf{x}_I$	current position of FE node (control point); may not lie on $\mathcal{S}^h$
$\mathbf{X}_I$	initial position of FE node (control point); may not lie on $\mathcal{S}_0^h$
$\boldsymbol{x}_I$	$= \sum_J N_J(\boldsymbol{\xi}_I)\mathbf{x}_J$; closest surface point of $\mathbf{x}_I$
$\boldsymbol{X}_I$	$= \sum_J N_J(\boldsymbol{\xi}_I)\mathbf{X}_J$; closest surface point of $\mathbf{X}_I$
$\mathbf{x}^e$	stacked array of all nodal $\mathbf{x}_I$ of finite element Ω^e
$\mathbf{X}^e$	stacked array of all nodal $\mathbf{X}_I$ of finite element Ω^e
$\mathbf{x}$	stacked array of all nodal $\mathbf{x}_I$ in the system
$\mathbf{X}$	stacked array of all nodal $\mathbf{X}_I$ in the system
ξ^α	convective surface coordinates; $\alpha = 1, 2$
$\boldsymbol{\xi}$	$= [\xi^1, \xi^2]$
Ω^e	finite element e in the current configuration
Ω^e_0	finite element e in the initial configuration
$\Omega^e_\square$	finite element e in the parametric domain $\mathcal{P}$
$\bar{\ldots}$	corresponding quantity of the material reconstruction mesh; e.g. $\bar{\Omega}^e$, $\bar{x}_I$, $\bar{\mathbf{x}}^e$

1 Introduction

Material modeling and design are rapidly advancing in many fields of engineering. This creates a demand for the a priori knowledge of material properties. Many modern materials, including textiles, concrete, composites and biological materials, are characterized by heterogeneity. This local change of the material properties can result from microstructure, imperfections, damage, or manufacturing processes. The characterization of heterogeneous materials is often inaccessible through standard testing methods (Wineman et al., 1979; Pierron and Grédiac, 2021). This is a particular difficulty in soft biological materials, since they present a unique set of challenges to experimental material identification procedures, such as their small size and delicate structure, the restricted access to representative samples, the difficult mounting of specimens, the provision of physiological conditions, as well as the obtainment of formal, ethical and medical consent (Evans, 2017). Therefore, nondestructive *in vivo* experiments, accompanied by numerical models and *in silico* inverse identification offer a path to overcome these challenges. Seminal work in this direction has been done on skin tissue (Vossen, 1994), heart muscles (Moulton et al., 1995), aortic aneurysms (Raghavan and Vorp, 2000), tympanic membranes (Aernouts and Dirckx, 2011), and abdominal walls (Simón-Allué et al., 2017).

Various inverse identification methods have been developed in the past in conjunction with digital image correlation systems (DIC) that provide full-field data, e.g. see Avril et al. (2008). The first class of inverse identification methods are *direct inverse* methods. They are based on the principle that material properties can be expressed explicitly in terms of the strain and stress components. Due to their high efficiency, these methods are favored in patient-specific rupture risk assessment, especially for vascular disorders, which are characterized by localized changes in wall composition and structure (Bersi et al., 2016). An example for a direct inverse method, is the Pointwise Identification Method (Zhao, 2009). It assumes that the local material properties follow directly from the local stress-strain data. It has been used to identify heterogeneous, anisotropic properties of planar soft tissues (Zhao et al., 2011; Genovese et al., 2014; Davis et al., 2015). Another direct inverse method is Local Extensional Stiffness Identification (LESI) proposed by Farzaneh et al. (2019a,b). It is based on the local membrane equilibrium equations, and has been applied to the identification of regional elastic properties. The Virtual Field Method (VFM) proposed by Pierron and Grédiac (2012), a popular direct inverse method based on the principle of virtual work, has been developed and used by many researchers for the identification of material parameters in homogeneous and heterogeneous linear elasticity (Avril et al., 2004; Avril and Pierron, 2007), hyperelasticity (Avril et al., 2010; Bersi et al., 2016; Marek et al., 2017), plasticity (Pierron et al., 2010; Martins et al., 2018) and incompressible elasticity (Mei and Avril, 2019).

The second class of inverse identification methods are *iterative inverse* methods, such as the Finite Element Model Updating method (FEMU) (Kavanagh and Clough, 1971), which minimizes the discrepancy between experimental measurements and finite element model predictions in a global least-squares sense. It is a well established technique associated with high robustness and low sensitivity to measurement noise, capable to model complex mechanical tests and structures (Goenezen et al., 2012). However, it requires a priori knowledge of boundary conditions and, due to its iterative character, can be computationally expensive. FEMU has been used for the identification of homogeneous hyperelastic solids (Iding et al., 1974), membranes (Kyriacou et al., 1997), nonlinear viscoelastic continua (Kauer et al., 2002), linear elastic continua (Oberai et al., 2003), as well as various anisotropic hyperelasticity models (Genovese et al., 2006; Bischoff et al., 2009; Badel et al., 2012; Wittek et al., 2013). Although FEMU was successfully used to identify homogeneous material models, to the best of our knowledge only few attempts have been made to deal with the heterogeneous distribution of material parameters. Seshaiyer and

Humphrey (2003) assumed homogeneity in sub-domains to identify material parameters based on the Neo-Hookean, Mooney-Rivlin and Fung models. A similar approach was used by Khalil et al. (2006) to identify the elastic properties of vascular tissues. Kroon and Holzapfel (2008, 2009) and Kroon (2010a) applied FEMU to determine element-wise constant material distributions of anisotropic nonlinear membranes. This formulation was extended by Kroon (2010b) to more general material distributions. The work by Kroon seems to be the most recent on FEMU for heterogeneous materials.

Many soft materials consist of thin, surface-like structures that can be efficiently described by *rotation-free* shell and membrane models, especially in the context of Isogeometric analysis (IGA) (Hughes et al., 2005). Such models require no rotational degrees of freedom. Further, compared to classical finite element methods (FEM), IGA exhibits higher accuracy and robustness per degree of freedom in many areas of computational mechanics (De Lorenzis et al., 2014; Nguyen et al., 2015; Schillinger, 2018). This is due to the fact that IGA discretizations can provide smoothness of any order across element boundaries, while no Gibbs oscillations appear in high order elements (Hughes et al., 2005). Furthermore, IGA can be integrated straightforwardly into existing FE software using the Bézier extraction operator (Borden et al., 2011; Scott et al., 2011). Due to its accurate yet efficient geometrical description with relatively few elements, IGA has become a particularly advantageous computational tool for shell structures.

A number of shell and membrane formulations using IGA have been proposed for both linear and nonlinear deformation regimes, see e.g. Kiendl et al. (2009); Nguyen-Thanh et al. (2011); Benson et al. (2011); Sauer et al. (2014); Tepole et al. (2015); Guo and Ruess (2015); Kiendl et al. (2015). IGA has been applied to inverse problems such as shape optimization (Wall et al., 2008; Manh et al., 2011; Kiendl et al., 2014), topology optimization (Seo et al., 2010; Dedè et al., 2012; Wang et al., 2018), load reconstruction (Vu-Bac et al., 2018, 2019) and material identification (Dufour et al., 2015; Do et al., 2019). To the best of our knowledge, Tepole et al. (2015) are the first to consider isogeometric Kirchhoff–Love shells for biological materials. In their approach, numerical integration through the shell thickness is used to obtain shell material models. On the other hand, Roohbakhshan and Sauer (2017) propose an analytical integration approach for biomaterial models to obtain direct surface models for Kirchhoff–Love shells. The application of isogeometric shell formulations to the forward and inverse simulation of biological materials can be expected to play an important role in the future.

In this paper, we propose a FEMU framework based on direct isogeometric shell formulations and gradient-based optimization, aimed at identifying the heterogeneous distribution of material properties. Large deformation incompressible isotropic material behavior is considered, since it is a basis for many soft material and biological tissue models. Our framework is most closely related to the approach by Kroon (2010b), which we extend here by adding isogeometric shell formulations and FE mesh-independent heterogeneity descriptions. The latter allow for more flexibility and efficiency in the inverse analysis. In particular, the proposed use of low order Lagrange interpolation is better suited for capturing material discontinuities than the high order IGA discretization used for rotation-free shell analysis. To the best of our knowledge, such a flexible meshing approach has not been considered in IGA-based inverse analysis before. The proposed inverse method contains the following features:

- Isogeometric shell FE formulation based on separate membrane and bending contributions derived from analytical thickness integration.
- Material discretization capable of capturing general material distributions independently from the FE analysis mesh.
- General Finite Element Model Updating inverse framework capable of reconstructing distributed constitutive parameters.
- Analytical sensitivities and Jacobians w.r.t. the design variables.

- Discussion of various error sources and strategies to reduce their influence.
- Systematic investigation of the influence of noise on the nonlinear material behavior.

The remainder of this paper is organized as follows: In Sec. 2 rotation-free thin shell theory is summarized. Sec. 3 presents the finite element discretization of the shell equations and the distributed material parameter field. A general framework for inverse analysis is proposed in Sec. 4, which is followed by several numerical examples in Sec. 5 to illustrate the capability of the identification protocol. The paper concludes with Sec. 6.

2 Thin shell theory

This section briefly summarizes the nonlinear theory of rotation-free Kirchhoff-Love shells in the framework of curvilinear coordinates. The formulation admits arbitrary hyperelastic material laws with general decomposition into bending and membrane contributions. A more detailed presentation can be found in Sauer (2018).

2.1 Surface description and kinematics

The shell surface, denoted $\mathcal{S}$, is characterized by the parametric description

$$\boldsymbol{x} = \boldsymbol{x}(\xi^\alpha), \quad \alpha = 1, 2\ , \tag{1}$$

where ξ^α are *curvilinear* coordinates associated with a 2D parameter domain $\mathcal{P}$. In the following, lower case symbols are used to denote kinematical quantities in the current configuration $\mathcal{S}$, while upper case symbols are used for the reference configuration $\mathcal{S}_0$. The tangent vectors to coordinate ξ^α at point $\boldsymbol{x} \in \mathcal{S}$ (corresponding to $\boldsymbol{X} \in \mathcal{S}_0$) are given by

$$\boldsymbol{a}_\alpha = \frac{\partial \boldsymbol{x}}{\partial \xi^\alpha}\,, \qquad \boldsymbol{A}_\alpha = \frac{\partial \boldsymbol{X}}{\partial \xi^\alpha}\ , \tag{2}$$

which form a basis. It is characterized by the surface metric, that has the covariant components

$$a_{\alpha\beta} = \boldsymbol{a}_\alpha \cdot \boldsymbol{a}_\beta\,, \qquad A_{\alpha\beta} = \boldsymbol{A}_\alpha \cdot \boldsymbol{A}_\beta\ . \tag{3}$$

Then the contravariant surface metric $[a^{\alpha\beta}] = [a_{\alpha\beta}]^{-1}$ and $[A^{\alpha\beta}] = [A_{\alpha\beta}]^{-1}$ can be evaluated, such that the contravariant base vectors are determined by [1]

$$\boldsymbol{a}^\alpha = a^{\alpha\beta}\boldsymbol{a}_\beta\,, \qquad \boldsymbol{A}^\alpha = A^{\alpha\beta}\boldsymbol{A}_\beta\,. \tag{4}$$

The normal unit vector to surface $\mathcal{S}$ can be obtained as

$$\boldsymbol{n} = \frac{\boldsymbol{a}_1 \times \boldsymbol{a}_2}{\|\boldsymbol{a}_1 \times \boldsymbol{a}_2\|}\,, \qquad \boldsymbol{N} = \frac{\boldsymbol{A}_1 \times \boldsymbol{A}_2}{\|\boldsymbol{A}_1 \times \boldsymbol{A}_2\|}\ . \tag{5}$$

Based on the second parametric derivative $\boldsymbol{a}_{\alpha,\beta} = \partial \boldsymbol{a}_\alpha / \partial \xi^\beta$ and $\boldsymbol{A}_{\alpha,\beta} = \partial \boldsymbol{A}_\alpha / \partial \xi^\beta$, the covariant curvature tensor components are given by

$$b_{\alpha\beta} = \boldsymbol{a}_{\alpha,\beta} \cdot \boldsymbol{n}\,, \qquad B_{\alpha\beta} = \boldsymbol{A}_{\alpha,\beta} \cdot \boldsymbol{N}\,. \tag{6}$$

The deformation map between $\mathcal{S}_0$ and $\mathcal{S}$, denoted $\boldsymbol{x} = \boldsymbol{\varphi}(\boldsymbol{X})$, is characterized by the surface deformation gradient

$$\boldsymbol{F} = \boldsymbol{a}_\alpha \otimes \boldsymbol{A}^\alpha \tag{7}$$

and the surface stretch

$$J = \frac{\sqrt{\det[a_{\alpha\beta}]}}{\sqrt{\det[A_{\alpha\beta}]}}\ . \tag{8}$$

---

[1] with summation from 1 to 2 implied over repeated Greek indices.

2.2 Weak form

The weak form of the shell,

$$G_{\mathrm{in}} + G_{\mathrm{int}} - G_{\mathrm{ext}} = 0 \qquad \forall\ \delta\boldsymbol{x} \in \mathcal{V}, \tag{9}$$

contains contributions from inertia as well as internal and external virtual work. The first is zero for quasi-static problems. The internal virtual work is given by

$$G_{\mathrm{int}} = \int_{\mathcal{S}_0} \frac{1}{2}\delta a_{\alpha\beta}\, \tau^{\alpha\beta} \mathrm{d}A + \int_{\mathcal{S}_0} \delta b_{\alpha\beta}\, M_0^{\alpha\beta} \mathrm{d}A\,, \tag{10}$$

where $\delta\boldsymbol{x} \in \mathcal{V}$ denotes a kinematically admissible variation of the position vector $\boldsymbol{x}$, while $\tau^{\alpha\beta}$ are the membrane stress components and $M_0^{\alpha\beta}$ are the bending moment components that can also be associated with the bending stresses. It is emphasized that $\tau^{\alpha\beta}$ and $M_0^{\alpha\beta}$ are not tensors, only tensor components. The full stress and moment tensors can be constructed by multiplying by the basis vectors from Eq. (2), but this is unnecessary for evaluating weak form (10). Both $\tau^{\alpha\beta}$ and $M_0^{\alpha\beta}$ are expressed w.r.t. reference surface configuration $\mathcal{S}_0$. The stress components w.r.t. the current configuration are $\sigma^{\alpha\beta} = \tau^{\alpha\beta}/J$ and $M^{\alpha\beta} = M_0^{\alpha\beta}/J$, where J is the surface stretch from Eq. (8). Further, $\delta a_{\alpha\beta}$ and $\delta b_{\alpha\beta}$ are the variations of the covariant surface metric and curvature tensor components, respectively.

The external work is given by

$$G_{\mathrm{ext}} = \int_{\mathcal{S}} \delta\boldsymbol{x} \cdot \boldsymbol{f}\, \mathrm{d}a + \int_{\partial_t\mathcal{S}} \delta\boldsymbol{x} \cdot \boldsymbol{t}\, \mathrm{d}s + \int_{\partial_m\mathcal{S}} \delta\boldsymbol{n} \cdot m_\tau\, \boldsymbol{\nu}\ \mathrm{d}s\ , \tag{11}$$

where $\boldsymbol{f} = \boldsymbol{f}_0 + p\,\boldsymbol{n}$ is a prescribed body force on $\mathcal{S}$ containing the dead load $\boldsymbol{f}_0$ and the external pressure p. Further, $\boldsymbol{t}$, m_τ and m_ν are distributed forces and moments prescribed along the edges, and $\boldsymbol{\nu} = \nu_\alpha \boldsymbol{a}^\alpha$ is the normal to edge $\partial_m\mathcal{S}$, where the bending moment m_τ is applied. In the following, the inertia term G_{in} is neglected. Due to its nonlinear character, the weak form needs to be linearized. Details on the linearization can be found in Sauer and Duong (2017).

2.3 Constitution

The constitutive relations for the shell can be either obtained via projection of 3D material laws onto the two-dimensional manifold (Roohbakhshan et al., 2016), or directly derived for surfaces. In the case of hyperelasticity the latter approach starts from a surface strain energy density function of the form

$$W = W(a_{\alpha\beta}, b_{\alpha\beta}) = W_{\mathrm{m}}(a_{\alpha\beta}) + W_{\mathrm{b}}(b_{\alpha\beta}, a_{\alpha\beta})\,, \tag{12}$$

where W_{m} is the membrane part that depends on the surface metric $a_{\alpha\beta}$, and W_{b} is the bending part that predominantly depends on the curvature tensor $b_{\alpha\beta}$ (Roohbakhshan and Sauer, 2017). Therefore, different constitutive models can be assigned for membrane deformation and bending.

Given the total strain energy

$$\Pi_{\mathrm{int}} = \int_{\mathcal{S}_0} W\, \mathrm{d}A\,, \tag{13}$$

the internal virtual work in (10) follows from the variation

$$G_{\mathrm{int}} = \delta\Pi_{\mathrm{int}} = \int_{\mathcal{S}_0} \delta W\, \mathrm{d}A\,, \tag{14}$$

since

$$\delta W = \frac{1}{2}\tau^{\alpha\beta}\delta a_{\alpha\beta} + M_0^{\alpha\beta}\delta b_{\alpha\beta} \tag{15}$$

for the stress and bending moment components

$$\tau^{\alpha\beta} = 2\frac{\partial W}{\partial a_{\alpha\beta}}\,, \qquad M_0^{\alpha\beta} = \frac{\partial W}{\partial b_{\alpha\beta}}\,, \tag{16}$$

that can be formally introduced through Cauchy's theorem (Sauer and Duong, 2017). Introducing the strains and relative curvatures

$$\varepsilon_{\alpha\beta} := \tfrac{1}{2}(a_{\alpha\beta} - A_{\alpha\beta})\,, \qquad \kappa_{\alpha\beta} := b_{\alpha\beta} - B_{\alpha\beta}\,, \tag{17}$$

one can also consider strain energy functions in the form $W = W(\varepsilon_{\alpha\beta}, \kappa_{\alpha\beta})$ and use

$$\tau^{\alpha\beta} = \frac{\partial W}{\partial \varepsilon_{\alpha\beta}}\,, \qquad M_0^{\alpha\beta} = \frac{\partial W}{\partial \kappa_{\alpha\beta}}\,, \tag{18}$$

since $\delta\varepsilon_{\alpha\beta} = \delta a_{\alpha\beta}/2$ and $\delta\kappa_{\alpha\beta} = \delta b_{\alpha\beta}$.

2.3.1 Initially planar shells

For initially planar shells, a simple choice is the 2-(material-)parameter formulation based on the Canham bending model (Canham, 1970) and the nonlinear incompressible Neo-Hookean membrane model (Sauer et al., 2014). This results in the membrane stress [2]

$$\tau^{\alpha\beta} = \mu\left(A^{\alpha\beta} - \frac{a^{\alpha\beta}}{J^2}\right)\,, \tag{19}$$

and the bending moment

$$M_0^{\alpha\beta} = c\,J\,b^{\alpha\beta}\,, \tag{20}$$

where the two material parameters μ and c, characterize the in-plane shear stiffness and the out-of-plane bending stiffness, respectively. According to the Canham model, the bending moment is linear w.r.t. the curvature component $b^{\alpha\beta}$, however, $b^{\alpha\beta}$ is nonlinear w.r.t. $b_{\alpha\beta}$, which implies a nonlinear bending model with non-constant bending stiffness. The corresponding material tangents are given in Sauer and Duong (2017). Since Eqs. (19) and (20) result from a surface strain energy, they require no further thickness integration. Instead, thickness integration is inherent to (19) and (20), so that the unit of μ (and likewise $\tau^{\alpha\beta}$) is [N/m], while the unit of c is [Nm] (and the unit of $M_0^{\alpha\beta}$ is [Nm/m]).[3] In principle μ and c can be treated fully independent from each other. But given the shell thickness T, c and μ can both be related to the material parameters of 3D elasticity, e.g. Young's modulus E and Poisson's ratio ν, e.g. see Duong et al. (2017).

2.3.2 Initially curved shells

For initially curved shells, a simple choice is the Koiter model (Ciarlet, 2005; Steigmann, 2013)

$$\tau^{\alpha\beta} = c^{\alpha\beta\gamma\delta}\varepsilon_{\gamma\delta}\,, \tag{21}$$

$$M_0^{\alpha\beta} = \frac{T^2}{12}c^{\alpha\beta\gamma\delta}\kappa_{\gamma\delta}\,, \tag{22}$$

---

[2] There is also a stress contribution coming from the Canham bending model (Sauer and Duong, 2017), but it is negligible for thin shells.

[3] In case basis $\boldsymbol{a}_\alpha$ has no units. On the other hand, if $\boldsymbol{a}_\alpha$ has units of length, $\tau^{\alpha\beta}$ and $M_0^{\alpha\beta}$ adjust accordingly.

with

$$
\begin{aligned}
c^{\alpha\beta\gamma\delta} &:= \Lambda\, \mathrm{I}_{\mathrm{dil}}^{\alpha\beta\gamma\delta} + 2\,\mu\, \mathrm{I}_{\mathrm{dev}}^{\alpha\beta\gamma\delta}\,, \\
\mathrm{I}_{\mathrm{dil}}^{\alpha\beta\gamma\delta} &:= A^{\alpha\beta} A^{\gamma\delta}\,, \\
\mathrm{I}_{\mathrm{dev}}^{\alpha\beta\gamma\delta} &:= \frac{1}{2}\big(A^{\alpha\gamma}A^{\beta\delta} + A^{\alpha\delta}A^{\beta\gamma}\big)\,,
\end{aligned}
\tag{23}
$$

where μ and Λ are the 2D Lamé parameters. They can be obtained, e.g., by analytical integration of the 3D Saint Venant-Kirchhoff model over the shell thickness T. This gives

$$
\mu = T\,\tilde{\mu}\,, \qquad \Lambda = T\,\frac{2\,\tilde{\Lambda}\,\tilde{\mu}}{\tilde{\Lambda} + 2\,\tilde{\mu}}\,, \tag{24}
$$

where $\tilde{\Lambda}$ and $\tilde{\mu}$ are the Lamé parameters in 3D elasticity. They are related to Young's modulus E and Poisson's ratio ν by

$$
\tilde{\mu} = \frac{E}{2(\nu+1)}\,, \qquad \tilde{\Lambda} = \frac{2\,\tilde{\mu}\,\nu}{(1-2\,\nu)}\,. \tag{25}
$$

For incompressible materials $\nu = 0.5$, leading to

$$
\mu = \frac{E\,T}{3}\,, \qquad \Lambda = 2\,\mu\,, \tag{26}
$$

such that

$$
c^{\alpha\beta\gamma\delta} = \frac{2\,E\,T}{3}\mathrm{I}^{\alpha\beta\gamma\delta}\,, \qquad \mathrm{I}^{\alpha\beta\gamma\delta} = \mathrm{I}_{\mathrm{dil}}^{\alpha\beta\gamma\delta} + \mathrm{I}_{\mathrm{dev}}^{\alpha\beta\gamma\delta}\,. \tag{27}
$$

3 FE discretization

This section presents the finite element discretization of the weak form on the basis of isogeometric analysis (IGA) to obtain the FE forces and the FE equilibrium equation following Sauer et al. (2014) and Duong et al. (2017). Subsequently, the discretization of the material and its synchronization with the FE analysis mesh is discussed.

3.1 Surface discretization

In order to discretize surface $\mathcal{S}$ and to approximately solve Eq. (9), NURBS-based shape functions proposed by Hughes et al. (2005) are used. They take the form

$$
N_I(\xi^\alpha) = \frac{w_I \hat{N}_I^e(\xi^\alpha)}{\sum_{I=1}^{n_e} w_I \hat{N}_I^e(\xi^\alpha)}\,, \tag{28}
$$

where $\{\hat{N}_I^e\}_{I=1}^{n_e}$ are the n_e B-spline basis functions of finite element Ω_e. They are the entries of the matrix

$$
\hat{\mathbf{N}}^e(\xi^\alpha) = \mathbf{C}_1^e\,\mathbf{B}^e(\xi^1) \otimes \mathbf{C}_2^e\,\mathbf{B}^e(\xi^2)\,, \tag{29}
$$

containing the Bernstein polynomials $\mathbf{B}^e(\xi^\alpha)$ and the Bézier extraction operator $\mathbf{C}_\alpha^e$ (Borden et al., 2011). The geometry within an undeformed element Ω_0^e and its deformed counterpart Ω^e is then approximated from the position of control points $\mathbf{X}^e$ and $\mathbf{x}^e$, respectively[4], as

$$
\boldsymbol{X} \approx \boldsymbol{X}^h = \sum_{I=1}^{n_e} N_I\,\mathbf{X}_I = \mathbf{N}^e\,\mathbf{X}^e\,, \qquad \boldsymbol{x} \approx \boldsymbol{x}^h = \sum_{I=1}^{n_e} N_I \mathbf{x}_I = \mathbf{N}^e \mathbf{x}^e\,, \tag{30}
$$

---

[4] Uppercase characters are dedicated to the undeformed configuration, the lowercase characters to the deformed configuration.

where $\mathbf{N}^e(\xi^\alpha) = [N_1\mathbf{1}, N_2\mathbf{1}, ..., N_{n_e}\mathbf{1}]$ is an array composed of the NURBS shape functions of Eq. (28) and $\mathbf{1}$ is the identity matrix in d-dimensional space. Further, $\mathbf{X}_I$ is the initial and $\mathbf{x}_I$ is the current position of the FE node (control point). Likewise, the displacements within element Ω^e are interpolated as

$$\boldsymbol{u} \approx \boldsymbol{u}^h = \sum_{I=1}^{n_e} N_I\, \mathbf{u}_I = \mathbf{N}^e \mathbf{u}^e\,. \tag{31}$$

The covariant tangent vectors of the surface are then determined by

$$\boldsymbol{a}_\alpha = \frac{\partial \boldsymbol{x}}{\partial \xi^\alpha} \approx \mathbf{N}^e_{,\alpha}\, \mathbf{x}^e, \qquad \boldsymbol{A}_\alpha = \frac{\partial \boldsymbol{X}}{\partial \xi^\alpha} \approx \mathbf{N}^e_{,\alpha}\, \mathbf{X}^e\,, \tag{32}$$

and the variation of $\boldsymbol{x}$ and $\boldsymbol{a}_\alpha$ are expressed as

$$\delta\boldsymbol{x} \approx \mathbf{N}^e\, \delta\mathbf{x}^e, \qquad \delta\boldsymbol{a}_\alpha \approx \mathbf{N}^e_{,\alpha}\, \delta\mathbf{x}^e\,. \tag{33}$$

Based on this, the discretization of all kinematic quantities and their variations can be determined, see Duong et al. (2017).

Remark 1: In classic finite elements, the nodes are lying on the discretized surface $\mathcal{S}^h \approx \mathcal{S}$. In isogeometric analysis, where spline-based shape functions are used, the control points $\mathbf{X}_I$ and $\mathbf{x}_I$, in general, do not lie on the discretized surfaces $\mathcal{S}^h_0$ and $\mathcal{S}^h$, respectively, since surface approximation (30) is not interpolating the control points, i.e.

$$\boldsymbol{X}_I := \sum_J N_J(\xi^\alpha_I)\, \mathbf{X}_J \neq \mathbf{X}_I \tag{34}$$

due to the property $N_I(\xi^\alpha_J) \neq \delta_{IJ}$. This must be taken into account when displacements resulting from IGA are compared with displacements resulting from experiments.

3.2 Weak form discretization

The original weak form (9) now yields the discretized version

$$\sum_{e=1}^{n_\mathrm{el}} (G^e_\mathrm{int} + G^e_\mathrm{ext}) = 0 \qquad \forall\ \delta\mathbf{x} \in \mathcal{V}^h, \tag{35}$$

where n_el is the number of finite elements and G^e_int and G^e_ext are the elemental contributions to the internal and external virtual work, respectively. The former can be written as

$$G^e_\mathrm{int} = \delta\mathbf{x}_e\, \mathbf{f}^e_\mathrm{int} = \delta\mathbf{x}_e\, (\mathbf{f}^e_{\mathrm{int}\tau} + \mathbf{f}^e_{\mathrm{int}M})\,. \tag{36}$$

Here the internal FE force vectors due to membrane stress $\tau^{\alpha\beta}$ and bending moment $M_0^{\alpha\beta}$ are

$$\mathbf{f}^e_{\mathrm{int}\tau} = \int_{\Omega^e_0} \tau^{\alpha\beta}\, \mathbf{N}^\mathrm{T}_{,\alpha}\, \boldsymbol{a}_\beta\, \mathrm{d}A\,, \tag{37}$$

and

$$\mathbf{f}^e_{\mathrm{int}M} = \int_{\Omega^e_0} M_0^{\alpha\beta}\, \mathbf{N}^\mathrm{T}_{;\alpha\beta}\, \boldsymbol{n}\, \mathrm{d}A\,, \tag{38}$$

where $\mathbf{N}_{;\alpha\beta} := \mathbf{N}_{,\alpha\beta} - \Gamma^\gamma_{\alpha\beta}\mathbf{N}_{,\gamma}$ for $\Gamma^\gamma_{\alpha\beta} := \boldsymbol{a}_{\alpha,\beta} \cdot \boldsymbol{a}^\gamma$. G^e_ext follows as

$$G^e_\mathrm{ext} = \delta\mathbf{x}^\mathrm{T}_e \big(\mathbf{f}^e_{\mathrm{ext}0} + \mathbf{f}^e_{\mathrm{ext}p} + \mathbf{f}^e_{\mathrm{ext}t} + \mathbf{f}^e_{\mathrm{ext}m}\big)\,, \tag{39}$$

where the external FE force vectors are

$$\mathbf{f}^e_{\mathrm{ext}0} = \int_{\Omega^e_0} \mathbf{N}^{\mathrm{T}} \boldsymbol{f}_0 \,\mathrm{d}A\,, \qquad \mathbf{f}^e_{\mathrm{ext}p} = \int_{\Omega^e_0} \mathbf{N}^{\mathrm{T}} p\,\boldsymbol{n}\,\mathrm{d}a\,, \tag{40}$$

$$\mathbf{f}^e_{\mathrm{ext}t} = \int_{\partial_t\Omega^e_0} \mathbf{N}^{\mathrm{T}} \boldsymbol{t}\,\mathrm{d}s\,, \qquad \mathbf{f}^e_{\mathrm{ext}m} = \int_{\partial_m\Omega^e_0} \mathbf{N}^{\mathrm{T}}_{,\alpha}\,\nu^{\alpha}\,m_\tau\,\boldsymbol{n}\,\mathrm{d}s\,. \tag{41}$$

Here $\boldsymbol{f}_0$ is a constant surface force, p is an external pressure acting always normal to $\mathcal{S}$, $\boldsymbol{t}$ is the effective boundary traction on $\partial_t\Omega^e_0 \subset \partial_t\mathcal{S}^h$, ν^α is the component of the unit normal to edge $\partial\mathcal{S}$, and m_τ is the tangential bending moment component on $\partial_m\Omega^e_0 \subset \partial_m\mathcal{S}^h$. The corresponding tangent matrices can be found in Duong et al. (2017).
With the preceding equations, weak form (35) can be rewritten as

$$\delta\mathbf{x}^{\mathrm{T}}\left[\mathbf{f}_{\mathrm{int}} - \mathbf{f}_{\mathrm{ext}}\right] = 0, \quad \forall\,\delta\mathbf{x} \in \mathcal{V}^h\,, \tag{42}$$

where

$$\mathbf{f}_{\mathrm{int}} = \sum_{e=1}^{n_{\mathrm{el}}} \mathbf{f}^e_{\mathrm{int}}\,, \quad \mathbf{f}_{\mathrm{ext}} = \sum_{e=1}^{n_{\mathrm{el}}} \mathbf{f}^e_{\mathrm{ext}} \tag{43}$$

are obtained from the assembly of the corresponding elemental force vectors and $\mathcal{V}^h$ is the kinematically admissible set of all nodal variations $\delta\mathbf{x}$. These are zero for the nodes on the Dirichlet boundary $\partial_u\mathcal{S}^h$. For the remaining nodes, Eq. (42) implies

$$\mathbf{f}(\mathbf{u}) = \mathbf{f}_{\mathrm{int}} - \mathbf{f}_{\mathrm{ext}} = \mathbf{0}\,, \tag{44}$$

which is the discretized equilibrium equation that needs to be solved for the $d\,n_{\mathrm{no}}$ unknown components of the nodal displacement vector

$$\mathbf{u} = \begin{bmatrix} \boldsymbol{u}_1 \\ \boldsymbol{u}_2 \\ \vdots \\ \boldsymbol{u}_{n_{\mathrm{no}}} \end{bmatrix}\,. \tag{45}$$

Remark 2: In this formulation no mapping of derivatives between master and current configuration is required, also no introduction of a local Cartesian basis is needed.

3.3 Discretization of the material parameters

The material parameters, here shear modulus μ and bending modulus c, or Young's modulus E and thickness T, are defined over the surface $\mathcal{S}_0$ as a continuous scalar field $q(\xi^\alpha)$ that is approximated within the material parameter element $\bar{\Omega}^{\bar{e}}$, by $\bar{n}_e$ nodal values q_I and interpolation functions $\bar{N}_I$ as

$$q = q(\xi^\alpha) \approx q^h = \sum_{I=1}^{\bar{n}_e} \bar{N}_I(\xi^\alpha)\,q_I = \bar{\mathbf{N}}^{\bar{e}}\mathbf{q}^{\bar{e}}\,, \tag{46}$$

where $\bar{\mathbf{N}}^{\bar{e}} := [\bar{N}_1, \bar{N}_2, \dots, \bar{N}_{\bar{n}_e}]$ and $\mathbf{q}^{\bar{e}} := [q_1, q_2, \dots, q_{\bar{n}_e}]^{\mathrm{T}}$ are the elemental arrays containing all elemental $\bar{N}_I$ and q_I. In this work, q is discretized with quadrilateral 4-node elements with bilinear Lagrange interpolation functions $\bar{N}_I$, see Fig. 1. In principle, other interpolation functions can be chosen for the material, however we restrict ourselves to bilinear interpolation here, as it provides a good starting point to capture the a priori unknown material distribution. Only if some a priori information about the material is known other possibilities can be justified

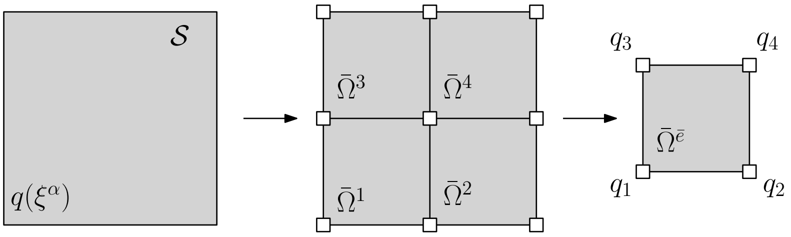

Figure 1: Approximation of the material parameter field q on surface $\mathcal{S}$ by 4-noded material elements $\bar{\Omega}^{\bar{e}}$.

as better choices. An example are material discontinuities, where constant interpolation might be preferable. Analogously to (45), the global vector

$$\mathbf{q} = \begin{bmatrix} \boldsymbol{q}_1 \\ \boldsymbol{q}_2 \\ \vdots \\ \boldsymbol{q}_{\bar{n}_{\text{no}}} \end{bmatrix} \tag{47}$$

is introduced. It contains the $n_{\text{var}} = \bar{d}\,\bar{n}_{\text{no}}$ unknown nodal material parameters to be identified by inverse analysis. Here, each node contains $\bar{d} = 2$ unknown design variables.

Before discussing this, the relation between the two different discretizations for $\mathbf{u}$ and $\mathbf{q}$ needs to be addressed, see Fig. 2. Conforming meshes consisting of rectangular elements in the parameter domain $\mathcal{P}(\xi^1, \xi^2)$ are considered here, which preserve the relation $\Omega^e_\square \subset \bar{\Omega}^{\bar{e}}_\square$, where $\Omega^e_\square$ and $\bar{\Omega}^{\bar{e}}_\square$ are the element domains in $\mathcal{P}$ for the analysis and material mesh respectively. This is also the domain where the numerical integration of the elemental FE force vectors in (37) and (38) is carried out. The tensor product structure of NURBS in (29) automatically leads to rectangular analysis elements on $\mathcal{P}$. Choosing conforming material elements is then a natural choice. In order to relate the two element domains, analysis element $\Omega^e_\square$, with its NURBS-based shape functions $\mathbf{N}(\xi^\alpha)$, is defined on the domain $\xi^\alpha \in [-1, 1]$, while the material element $\bar{\Omega}^{\bar{e}}_\square$, with its Lagrange shape functions $\bar{\mathbf{N}}(\bar{\xi}^\alpha)$, is defined on domain $\bar{\xi}^\alpha \in [-1, 1]$. The mapping between domains $\xi^\alpha \mapsto \bar{\xi}^\alpha$ is obtained by affine linear transformation, i.e.

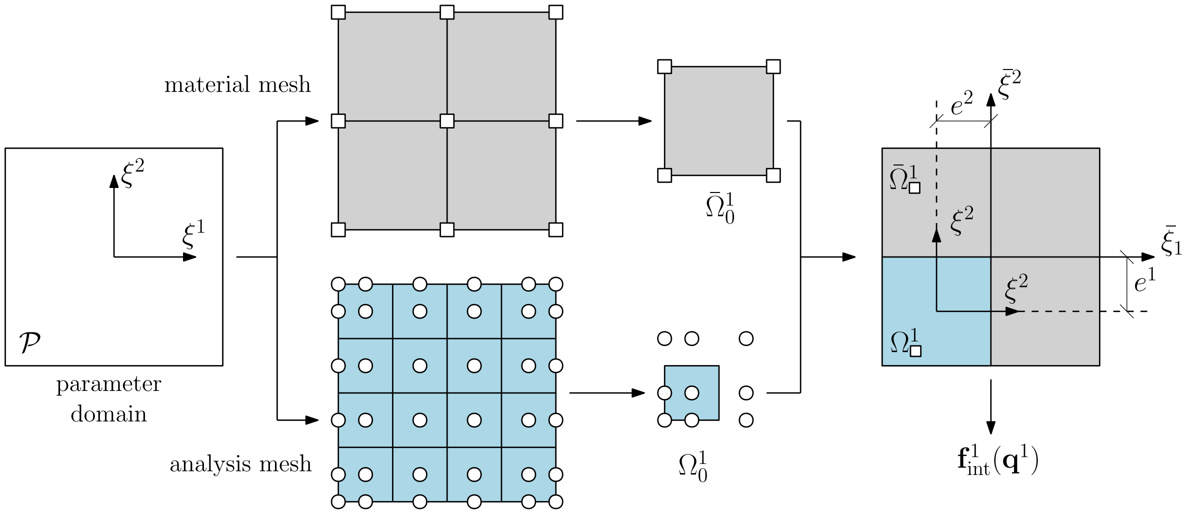

Figure 2: Example of mapping $\xi^\alpha \mapsto \bar{\xi}^\alpha$ for element $\Omega^1_\square \subset \bar{\Omega}^1_\square$. In this example $n_{\text{el}} = 16$, $\bar{n}_{\text{el}} = 4$, $n_1 = n_2 = 2$ and $e^1 = e^2 = 1$.

$$[\bar{\xi}^1, \bar{\xi}^2] = \left[\frac{1}{n_1}\left(\xi^1 + e^1\right), \frac{1}{n_2}\left(\xi^2 + e^2\right)\right] , \tag{48}$$

such that $\bar{N}_I = \bar{N}_I\big(\bar{\xi}^\alpha(\xi^\beta)\big)$ becomes a function of ξ^β. Here e^α is the offset between the coordinate centers of $\bar{\Omega}_0^{\bar{e}}$ and Ω_0^e and n_α is the number of $\Omega_0^e \subset \bar{\Omega}_0^{\bar{e}}$ in direction α (see Fig. 2).

4 Inverse analysis

In this section the inverse problem is formulated in the context of optimization. A corresponding optimization algorithm and optimality conditions are discussed, followed by an investigation of the different error sources that affect the precision of the inverse problem solution. Finally, the analytical sensitivities for the considered constitutive parameters are derived.

4.1 Objective function

The Finite Element Model Updating method is used to solve the inverse problem. Accordingly, the unknown design vector $\mathbf{q}$ is obtained from the constrained minimization

$$\min_{\mathbf{q}} f(\mathbf{q}) \tag{49}$$

subject to the bounds $0 < q_{\min} \leq q_I \leq q_{\max}$ and subject to satisfying the discrete weak form (42). f is a scalar-valued function known as the *objective function*. It depends on the $\bar{d}\,\bar{n}_{\text{no}}$ nodal values of the $\bar{d}$ discretized constitutive parameters $q(\xi^\alpha)$ according to interpolation (46). The function f expresses the discrepancy between the model and the observed experimental behavior. The least squares form

$$f(\mathbf{q}) = \frac{\|\mathbf{U}_{\text{exp}} - \mathbf{U}_{\text{FE}}(\mathbf{q})\|^2}{2\,\|\mathbf{U}_{\text{exp}}\|^2} + \frac{\|\mathbf{R}_{\text{exp}} - \mathbf{R}_{\text{FE}}(\mathbf{q})\|^2}{2\,\|\mathbf{R}_{\text{exp}}\|^2} \tag{50}$$

is considered, where

$$\mathbf{U}_{\text{exp}} = \begin{bmatrix} \boldsymbol{u}_1^{\text{exp}} \\ \boldsymbol{u}_2^{\text{exp}} \\ \vdots \\ \boldsymbol{u}_{n_{\text{exp}}}^{\text{exp}} \end{bmatrix} \tag{51}$$

is a vector containing the n_{exp} experimentally measured displacements $\boldsymbol{u}_I^{\text{exp}}, I = 1, \ldots, n_{\text{exp}}$, at location $\boldsymbol{x}_I^{\text{exp}} \in \mathcal{S}$ and

$$\mathbf{U}_{\text{FE}}(\mathbf{q}) = \begin{bmatrix} \boldsymbol{u}^h\big(\boldsymbol{x}_1^{\text{exp}}, \mathbf{q}\big) \\ \boldsymbol{u}^h\big(\boldsymbol{x}_2^{\text{exp}}, \mathbf{q}\big) \\ \vdots \\ \boldsymbol{u}^h\big(\boldsymbol{x}_{n_{\text{exp}}}^{\text{exp}}, \mathbf{q}\big) \end{bmatrix}, \tag{52}$$

is a vector containing the corresponding n_{exp} FE results at $\boldsymbol{x}_I^{\text{exp}}$, which according to Eq. (31) are

$$\boldsymbol{u}^h\big(\boldsymbol{x}_I^{\text{exp}}, \mathbf{q}\big) = \mathbf{N}^e\big(\boldsymbol{x}_I^{\text{exp}}\big)\,\mathbf{u}^e(\mathbf{q})\,. \tag{53}$$

Thus (49) determines the material distribution $\mathbf{q}$ that minimizes the difference between n_{exp} measured displacements $\boldsymbol{u}_I^{\text{exp}}$ and their numerically calculated counterparts. The n_{exp} measurements can come from a single experiment or from multiple experiments that are for example conducted at n_{ll} different load levels and concatenated in the global vector $\mathbf{U}$. This is useful for capturing the nonlinear response of $\mathbf{U}_{\text{FE}}$ on $\mathbf{q}$ for increasing loads, as is seen in the examples of Sec. 5. Additionally, to ensure that system (49) is uniquely determinable for pure Dirichlet problems, the reaction forces on various boundaries are included in objective (50) via vector $\mathbf{R}$. Without support reactions, each material parameter is only determinable up to a constant for pure Dirichlet problems.

4.2 Optimization algorithm

In order to satisfy Eq. (49), a trust-region method is employed (Conn et al., 2000). Trust region methods are iterative methods that construct an approximation of the function $f(\mathbf{q})$ in the neighborhood (trust region) $\mathcal{N}$ of the current iterate $\mathbf{q}_k$. One of the advantages of trust-region methods over line search methods, is that non-convex approximate models can be used, which makes this class of iterative methods reliable, robust and applicable to ill-conditioned problems (Yuan, 2000). Minimization over $\mathcal{N}$ (the trust-region subproblem) results in solution $\mathbf{s}_k$, called the trial step. The current design is then updated by $\mathbf{q}_k + \mathbf{s}_k$ if $f(\mathbf{q}_k + \mathbf{s}_k) < f(\mathbf{q}_k)$. Otherwise, it remains unchanged, $\mathcal{N}$ is shrunk and the computation of $\mathbf{s}_k$ is repeated. The algorithm keeps updating $\mathbf{q}_k$ until certain conditions are satisfied. The iteration is terminated when the two stopping criteria

$$|f(\mathbf{q}_{k+1}) - f(\mathbf{q}_k)| \leqslant \epsilon \tag{54}$$

$$\|\mathbf{q}_{k+1} - \mathbf{q}_k\| \leqslant \epsilon\,, \tag{55}$$

are satisfied. Here ϵ is a small positive tolerance chosen on the order of machine precision ($\epsilon \approx 2.2 \cdot 10^{-16}$). Together, both conditions ensure stopping the procedure after both f and $\mathbf{q}$ have converged. The `lsqnonlin` solver from the MATLAB Optimization Toolbox$^{\text{TM}}$ (MATLAB, 2018) is employed, which takes advantage of the Trust-region Interior Reflective (TIR) approach proposed by Coleman and Li (1996) and allows adding analytical Jacobians (see Appendix A). The flowchart of the inverse identification algorithm is shown in Fig. 3. Given a constitutive law, the initial estimate $\mathbf{q}_0$, the FE analysis mesh and material mesh are provided first. They are needed to define the material model, determine the mapping between material and FE mesh and

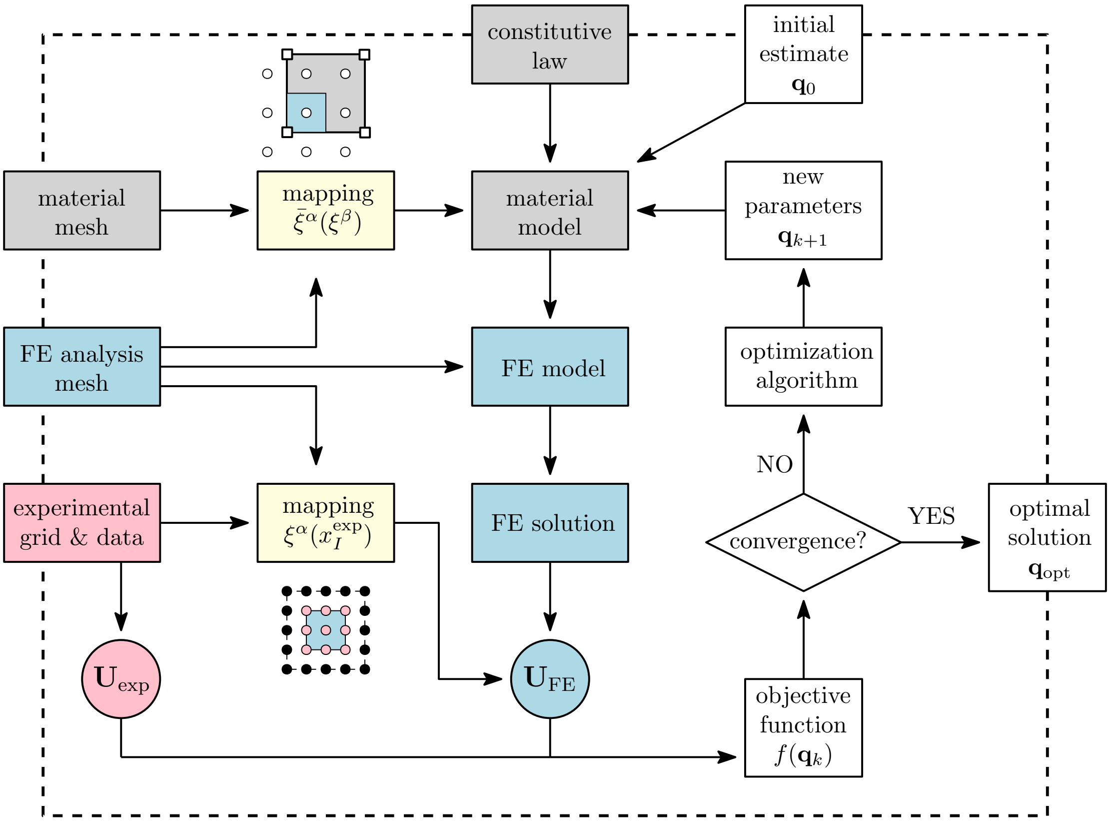

Figure 3: Flowchart of the material identification algorithm: Based on a chosen FE analysis mesh and chosen material mesh, the algorithm determines the optimal solution for the material parameters $\mathbf{q}$ for given initial guess $\mathbf{q}_0$, given experimental data and given constitutive law.

determine the FE solution. Next, the experimental data (experimental grid and measurements $\mathbf{U}_{\text{exp}}$) are provided. The mapping between experimental grid and FE mesh is determined, and used to compute the displacements $\mathbf{U}_{\text{FE}}$ at locations $\boldsymbol{x}_I^{\text{exp}}$. Given $\mathbf{U}_{\text{exp}}$ and $\mathbf{U}_{\text{FE}}$, the objective function $f(\mathbf{q})$ is evaluated. As long as the convergence criteria (54) & (55) are not met, the optimization algorithm proceeds to find a new estimate and repeats the process.

4.3 Error sources

The inverse identification process is based on three discretized fields, see Fig. 4: First, the FE discretization of the displacement field of the forward problem (31). It determines the FE accuracy and computational cost of the forward problem. Second, the material parameter discretization (46). It captures the material distribution and establishes the size and computational cost of the inverse problem (characterized by n_{var}). Third, the chosen experimental displacement grid. It determines the amount of available data points used in the inverse analysis, which also contributes to the computational cost of the inverse problem. There are three corresponding error sources:

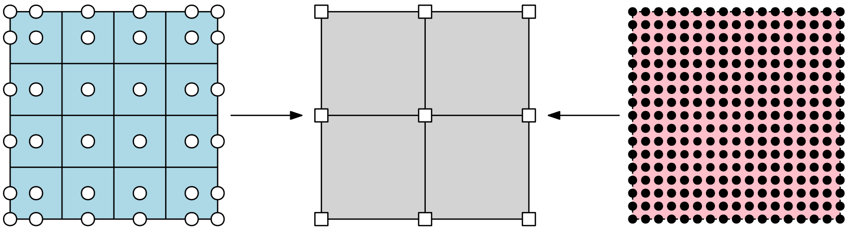

Figure 4: Inverse analysis based on three differently discretized fields: The central objective is to reconstruct the unknown parameters of the material mesh (*center*). This requires a sufficiently dense FE analysis mesh (*left*) and experimental grid (*right*).

- finite element approximation error, resulting from the difference between the finite element solution for the displacement and the (unknown) exact displacement field,
- material approximation error, resulting from the difference between the material interpolation and the (unknown) exact material distribution,
- experimental measurement error (i.e. noise), resulting from the difference between the measured data and the (unknown) exact specimen behavior.

The following numerical examples demonstrate that the proposed inverse algorithm converges w.r.t. all three error sources. For this, exact (or at least highly accurate) solutions are required. They are determined here by (1) conducting a convergence study of the forward FE problem, thus determining suitable FE meshes with acceptable error levels, (2) providing known material distributions, and (3) manufacturing “experimental” results based on highly accurate FE results and then mimicking the effect of measurement error through the subsequent application of random noise. The FE mesh for these synthetic results is always chosen much denser than the discretization used for the subsequent inverse analysis to avoid the analysis bias commonly referred to as *inverse crimes* (Colton and Kress, 1998; Wirgin, 2004). Further, by examining the sensitivities, preliminary conclusions on the nature of the inverse problem can be drawn.

4.4 Analytical sensitivities

Gradient-based optimization algorithms typically require the gradient $\mathbf{g}(\mathbf{q})$ and Hessian $\mathbf{H}(\mathbf{q})$ of the objective function. Often, those are approximated through computationally expensive finite differences. On the other hand, the available constitutive formulations and FE force vectors given in Sec. 2 & 3 allow for the derivation and implementation of the analytical gradient and Hessian. In order to provide the analytical gradient, differentiation of the internal FE force vectors in Eqs. (37) and (38) w.r.t. the elemental material parameter vector $\mathbf{q}^{\bar{e}}$ is needed. Denoting the elemental sensitivity matrix

$$\mathbf{S}^{e\bar{e}} := \frac{\partial \mathbf{f}^{e}_{\mathrm{int}}}{\partial \mathbf{q}^{\bar{e}}} \,, \tag{56}$$

and applying (46) to μ and c, the change of the internal force vector due to material changes becomes

$$\Delta \mathbf{f}^{e}_{\mathrm{int}} = \frac{\partial \mathbf{f}^{e}_{\mathrm{int}\tau}}{\partial \boldsymbol{\mu}^{\bar{e}}} \Delta \boldsymbol{\mu}^{\bar{e}} + \frac{\partial \mathbf{f}^{e}_{\mathrm{int}M}}{\partial \mathbf{c}^{\bar{e}}} \Delta \mathbf{c}^{\bar{e}} = \mathbf{S}^{e\bar{e}}_{\mu} \Delta \boldsymbol{\mu}^{\bar{e}} + \mathbf{S}^{e\bar{e}}_{c} \Delta \mathbf{c}^{\bar{e}} \ , \tag{57}$$

where

$$\mathbf{S}^{e\bar{e}}_{\mu} := \int_{\Omega^e_0} \mathbf{N}^{e\mathrm{T}}_{,\alpha} \boldsymbol{a}_{\beta} \left(A^{\alpha\beta} - \frac{a^{\alpha\beta}}{J^2} \right) \bar{\mathbf{N}}^{\bar{e}} \, \mathrm{d}A \tag{58}$$

and

$$\mathbf{S}^{e\bar{e}}_{c} := \int_{\Omega^e_0} J \, b^{\alpha\beta} \, \mathbf{N}^{e\mathrm{T}}_{;\alpha\beta} \, \boldsymbol{n} \, \bar{\mathbf{N}}^{\bar{e}} \, \mathrm{d}A \tag{59}$$

are the Neo-Hookean membrane and the Canham bending sensitivity, respectively, that follow directly from (37), (38), (19), (20), (46) and (56). For the Koiter model, (46) is applied to E and T. (57) then becomes

$$\Delta \mathbf{f}^{e}_{\mathrm{int}} = \frac{\partial \mathbf{f}^{e}_{\mathrm{int}}}{\partial \mathbf{E}^{\bar{e}}} \Delta \mathbf{E}^{\bar{e}} + \frac{\partial \mathbf{f}^{e}_{\mathrm{int}}}{\partial \mathbf{T}^{\bar{e}}} \Delta \mathbf{T}^{\bar{e}} = \mathbf{S}^{e\bar{e}}_{E} \Delta \mathbf{E}^{\bar{e}} + \mathbf{S}^{e\bar{e}}_{T} \Delta \mathbf{T}^{\bar{e}} \ , \tag{60}$$

where

$$\mathbf{S}^{e\bar{e}}_{E} := \int_{\Omega^e_0} \left(\frac{2\,T}{3} \mathbf{N}^{\mathrm{T}}_{,\alpha} \, \mathrm{I}^{\alpha\beta\gamma\delta} \, \varepsilon_{\gamma\delta} \, \boldsymbol{a}_{\beta} + \frac{T^3}{18} \, \mathbf{N}^{\mathrm{T}}_{;\alpha\beta} \, \mathrm{I}^{\alpha\beta\gamma\delta} \, \kappa_{\gamma\delta} \, \boldsymbol{n} \right) \bar{\mathbf{N}}^{\bar{e}} \, \mathrm{d}A \,, \tag{61}$$

$$\mathbf{S}^{e\bar{e}}_{T} := \int_{\Omega^e_0} \left(\frac{2E}{3} \mathbf{N}^{\mathrm{T}}_{,\alpha} \, \mathrm{I}^{\alpha\beta\gamma\delta} \, \varepsilon_{\gamma\delta} \, \boldsymbol{a}_{\beta} + \frac{E\,T^2}{6} \, \mathbf{N}^{\mathrm{T}}_{;\alpha\beta} \, \mathrm{I}^{\alpha\beta\gamma\delta} \, \kappa_{\gamma\delta} \, \boldsymbol{n} \right) \bar{\mathbf{N}}^{\bar{e}} \, \mathrm{d}A \,. \tag{62}$$

are the sensitivities w.r.t. Young's modulus E and shell thickness T, that follow from (37), (38), (21), (22), (27), (46) and (56).

All $\mathbf{S}^{e\bar{e}}_{\bullet}$ are of size[5] 27 × 4 and require numerical integration over element Ω^e_0 and subsequent assembly for all $e = 1, \ldots, n_{\mathrm{el}}$ and $\bar{e} = 1, \ldots, \bar{n}_e$. This results in the global sensitivity matrix $\mathbf{S}$ with dimension $d\,n_{\mathrm{no}} \times \bar{d}\,\bar{n}_{\mathrm{no}}$. If $\mathbf{f}^{e}_{\mathrm{int}}$ is linear in $\mathbf{q}$, the sensitivities are constant (in $\mathbf{q}$) and the global force vector is simply given by

$$\mathbf{f}_{\mathrm{int}} = \mathbf{S}\,\mathbf{q} \,, \tag{63}$$

which is the case for (58) and (59), but not (61) and (62). As seen in (58) and (59), the membrane and bending sensitivities depend differently on the deformation. Since the deformation varies in space and time, the two sensitivities can thus be expected to play different roles in space and time[6]. This is seen in the example of Sec. 5.3.

Given $\mathbf{S}$, the discretization of the gradient and Hessian follow as outlined in Appendix A.

---

[5] number of degrees of freedom for finite element e × number of material parameters per material element $\bar{e}$.

[6] or computational pseudo-time marking load stepping.

5 Numerical examples

In this section four different identification examples are examined: uniaxial tension in Sec. 5.1 – a pure membrane problem that according to (19) only depends on the unknown shear modulus μ, pure bending in Sec. 5.2, which according to (20) only depends on the unknown bending stiffness c, inflation in Sec. 5.3 – a coupled problem involving unknowns c and μ, and abdominal wall pressurization – a coupled problem involving unknowns E and T. Quasi experimental deformations are used in all cases. They are generated by accurately solving the forward problem defined by the given analytical reference distribution $q(\boldsymbol{X})$.[7] In order to mimic measurement uncertainties, random noise is added to the deformation obtained from the reference parameters such that the measured displacement is

$$u_{Ii}^{\mathrm{exp}} = u_i^h(\boldsymbol{x}_I^{\mathrm{exp}})(1+\gamma_{Ii})\,, \tag{64}$$

where $i = 1, 2, 3$ are the Cartesian components, u_i^h is the solution for a very fine FE mesh and each γ_{Ii} is a random number picked uniformly from the range $[-1, 1]$ and multiplied by the considered noise level, which is up to 4% in all examples.

5.1 Uniaxial tension

The first example considers uniaxial tension, which induces pure membrane deformations without any bending. It thus allows to study material reconstruction for a single ($\bar{d} = 1$) unknown field – in this example the shear modulus $\mu = \mu(\boldsymbol{X})$. To induce uniaxial tension, a flat sheet with dimension $L_x \times L_y = L \times L$ is fixed in all directions on the left edge ($X = 0$), fixed in the Z- direction on the entire surface, and stretched by the prescribed displacement $\bar{\boldsymbol{u}} = L\boldsymbol{e}_1$ applied to the opposite edge ($X = L$), see Fig. 5.

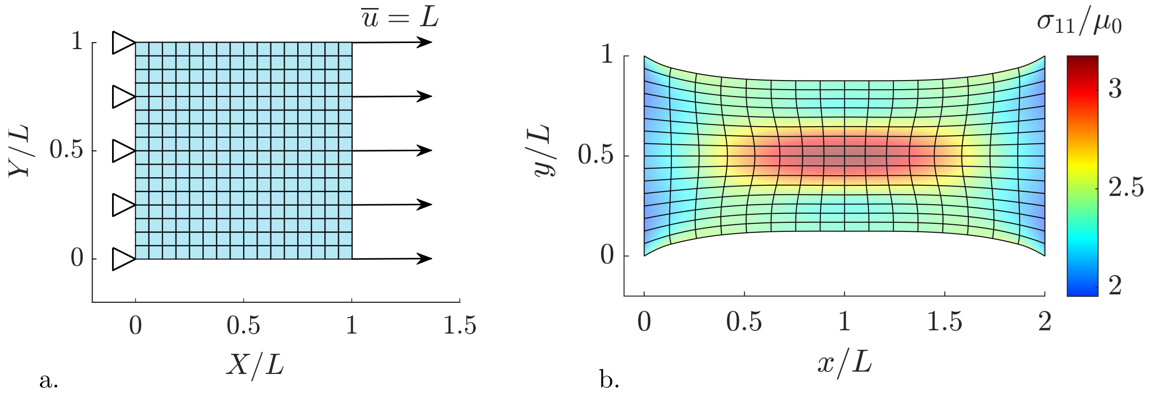

Figure 5: Uniaxial tension: a. undeformed configuration; b. deformed configuration colored by the membrane stress $\sigma_{11} = \boldsymbol{e}_1 \cdot \boldsymbol{\sigma}\boldsymbol{e}_1$, ranging between $1.96\mu_0$ and $3.17\mu_0$.

The incompressible Neo-Hooke model (19) is used with the heterogeneous reference shear modulus distribution

$$\mu_{\mathrm{ref}}(X,Y) = \begin{cases} \mu_0 & \text{for} \quad R \geq R_0\,, \\ \mu_0 + \dfrac{\Delta\mu_1}{2} \cdot \left(1 + \cos\left(\pi\dfrac{R}{R_0}\right)\right) & \text{for} \quad R < R_0\,, \end{cases} \tag{65}$$

where $\Delta\mu_1 = \mu_0$, $R^2 := X^2 + Y^2$ and $R_0 = 0.35L$, see Fig. 6a. L and μ_0 are used for normaliza-

---

[7] q can be equivalently expressed as a function of ξ^α, $\boldsymbol{x}$ or $\boldsymbol{X}$, since a 1-to-1 mapping between the three configurations is assumed here.

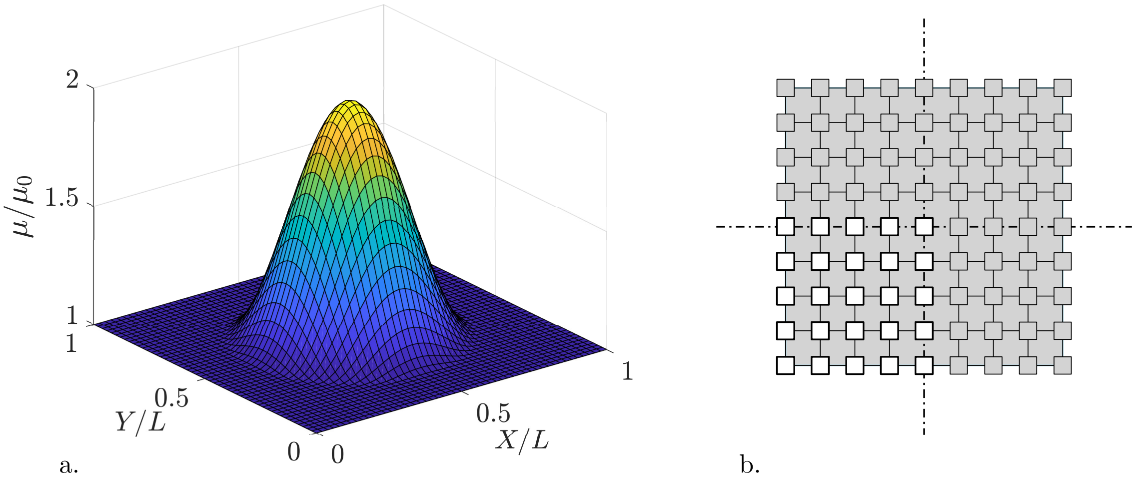

Figure 6: Uniaxial tension: a. reference shear modulus distribution $\mu(X, Y)$; b. material mesh $\bar{n}_{\mathrm{el}} = 8\times 8$, reduced to $n_{\mathrm{var}} = 25$ unknowns due to symmetry.

tion and do not need to be specified. Based on the separate convergence study shown in Fig. 7a, $n_{\mathrm{el}} = 16 \times 16$ FE are chosen for most of the following cases, since the FE analysis error is below $2.0 \cdot 10^{-4}$. As seen, the convergence rate is only linear for this example, even though quadratic NURBS are used. This is due to the four inherent corner singularities. If corner singularities are avoided, e.g. by fixing the Y-direction at the top and bottom edges ($Y = 0, Y = L$) the ideal convergence rate $O\big(n_{\mathrm{el}}^{-1.5}\big) = O(h^3)$ is obtained (Strang and Fix, 1973), see Fig. 7b.

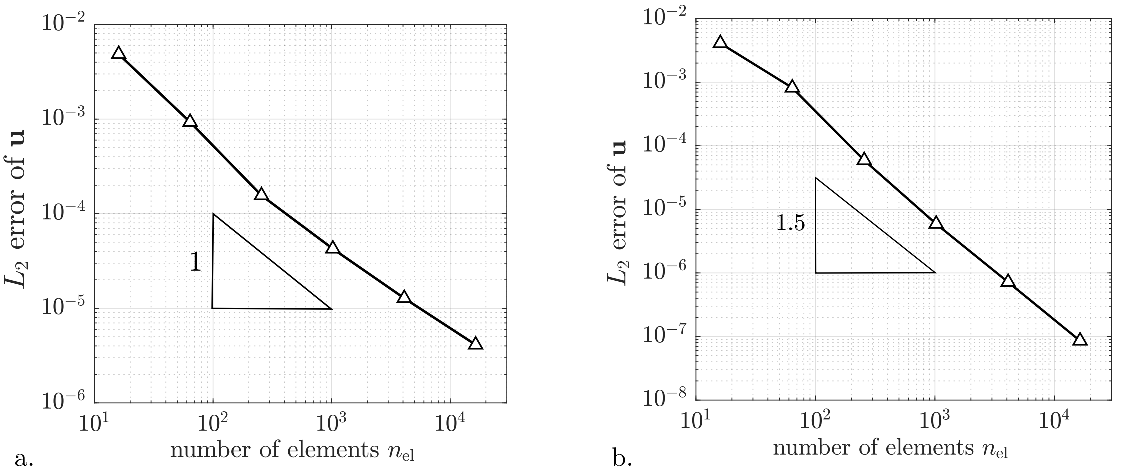

Figure 7: Uniaxial tension: a. FE convergence of the discrete L_2 error $\|\mathbf{u}_{\mathrm{exact}} - \mathbf{u}_{\mathrm{FE}}\|/\|\mathbf{u}_{\mathrm{exact}}\|$, where $\mathbf{u}_{\mathrm{exact}}$ is the FE solution for $n_{\mathrm{el}} = 512 \times 512$ elements; b. FE convergence for the case without corner singularities.

The material reconstruction mesh varies between $\bar{n}_{\mathrm{el}} = 8 \times 8$ ($n_{\mathrm{var}} = \bar{n}_{\mathrm{no}} = 9 \times 9$) and $\bar{n}_{\mathrm{el}} = 32 \times 32$ ($n_{\mathrm{var}} = \bar{n}_{\mathrm{no}} = 33 \times 33$). Exploiting symmetry, only 1/4 of the material elements can be used in this particular example to speed-up computations (see Fig. 6b). However, it should be noted that in general the material symmetry is not known a priori, and hence should not be used. The net reaction force R_x is included in the objection function in order to ensure that the problem is well-posed. Objective minimization is done with the chosen lower and upper bounds $\mu_{\mathrm{min}} = 0.1\,\mu_0$ and $\mu_{\mathrm{max}} = 5.0\,\mu_0$. The initial estimate is a vector of random numbers from the range $[\mu_{\mathrm{min}}, \mu_{\mathrm{max}}]$. The reconstruction results for different noise levels are presented in Tab. 1

in terms of the maximum, $\delta_{\max}$, and average, δ_{ave}, of the relative error

$$\delta_I = \left| \frac{q_{I,\text{ref}} - q_{I,\text{opt}}}{q_{I,\text{ref}}} \right|, \qquad I = 1, \dots, \bar{n}_{\text{no}} \tag{66}$$

between reference and estimated parameters. The error distribution for selected cases is shown in Fig. 8. As long as there is no noise, the error distribution is symmetric, even if symmetry is not exploited computationally, as is the case in Fig. 8.

Case	FE n_{el}	mat. $\bar{n}_{\text{el}}$	mat. n_{var}	exp. $n_{\text{exp}}/\text{n}_{\text{ll}}$	load n_{ll}	noise [%]	$\delta_{\max}$ [%]	δ_{ave} [%]
1.1	16 × 16	4 × 4	25	130^2	1	0	24.45	3.72
1.2	16 × 16	8 × 8	81	130^2	1	0	4.94	1.53
1.3	16 × 16	16 × 16	289	130^2	1	0	1.81	0.54
1.4	32 × 32	32 × 32	1089	130^2	1	0	1.18	0.24
1.5	16 × 16	8 × 8	25	130^2	1	1	5.64 ± 0.49	1.99 ± 0.17
1.6	16 × 16	8 × 8	25	514^2	1	1	5.01 ± 0.12	1.83 ± 0.031
1.7	16 × 16	8 × 8	25	130^2	1	2	6.34 ± 0.85	2.29 ± 0.23
1.8	16 × 16	8 × 8	25	130^2	2	2	6.22 ± 0.81	2.12 ± 0.16
1.9	16 × 16	8 × 8	25	514^2	2	2	5.08 ± 0.14	1.88 ± 0.039
1.10	16 × 16	8 × 8	25	514^2	2	4	5.29 ± 0.26	1.93 ± 0.072
1.11	16 × 16	8 × 8	25	514^2	4	4	5.05 ± 0.22	1.94 ± 0.064
1.12	16 × 16	16 × 16	289	514^2	4	4	16.21 ± 3.01	3.53 ± 0.54

Table 1: Uniaxial tension: Studied inverse analysis cases and their errors $\delta_{\max}$ and δ_{ave} for different FE meshes, material meshes, number of design variables, experimental grid resolutions, load levels and noise levels. At least 25 repetitions were used for the statistical analysis of Cases 1.5–1.12. The highlighted four cases are compared in Fig. 9b. Cases 1.5–1.11 use material mesh symmetry resulting in lower n_{var}.

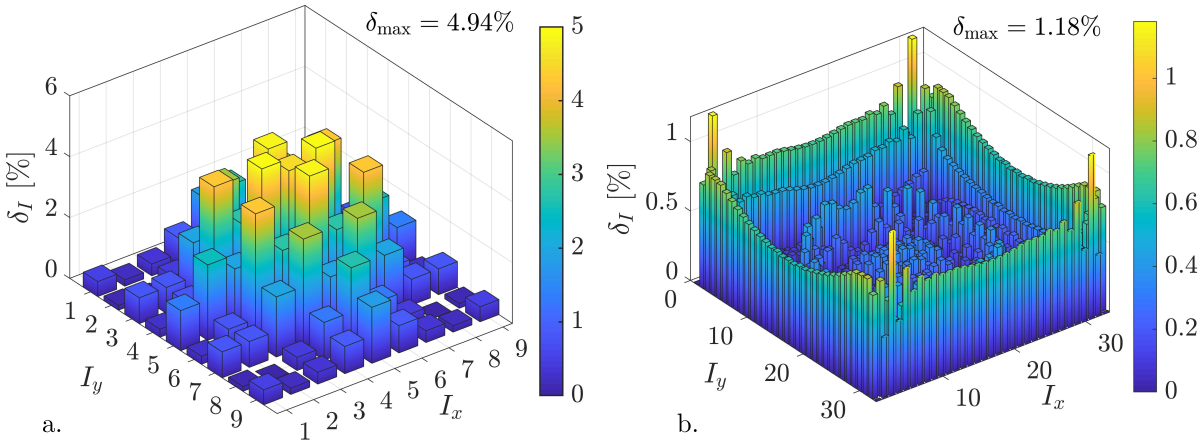

Figure 8: Uniaxial tension: Error between identified and reference μ_I values for: a. Case 1.2 with $n_{\text{var}} = 81$ unknowns; b. Case 1.4 with $n_{\text{var}} = 1089$ unknowns.

As Tab. 1 shows, for Cases 1.1–1.4 with 0% noise, the reconstruction error decreases when refining FE and material meshes – ultimately down to $\delta_{\text{ave}} = 0.24\%$ for Case 1.4 (also shown in Fig. 8b). The results are for $\Delta\mu_1 = \mu_0$. Other $\Delta\mu_1$ values, including $\Delta\mu_1 < 0$, give similar results. Case 1.2 has been repeated for various initial estimates resulting all in the same error distribution (Fig. 8a). Hence, no sensitivity w.r.t. the initial estimate is observed, and the

constant initial estimate $\mu = \mu_0$ is considered in all further cases.
Cases 1.5–1.12 examine the reconstruction for experimental data with the addition of 1–4% noise according to (64). The statistical effect of random noise is taken into account by repeating each case 25 times. Here, δ_{max} and δ_{ave} are obtained in each run, and then the mean and standard deviation of all δ_{max} and δ_{ave} are calculated, see Tab. 1.
The reconstruction algorithm is expected to overcome noise by incorporating a sufficient number of measurements into the objection function, either by refining the experimental grid or by increasing the number of considered load levels. This is confirmed by Cases 1.5–1.12. Eventually, a similar error is achieved for 4% noise (Case 1.11) as for zero noise (Case 1.2) when 514×514 experimental points and four load levels (25%, 50%, 75% and 100% of the load) are used. For Case 1.11 errors δ_{max} and δ_{ave} were found at $5.05 \pm 0.22\%$ (mean ± standard deviation) and $1.94 \pm 0.064\%$, respectively. The histogram of the average error δ_{ave} calculated from 100 runs for Case 1.11 is shown in Fig. 9a. As seen, the histogram is close to a normal distribution.

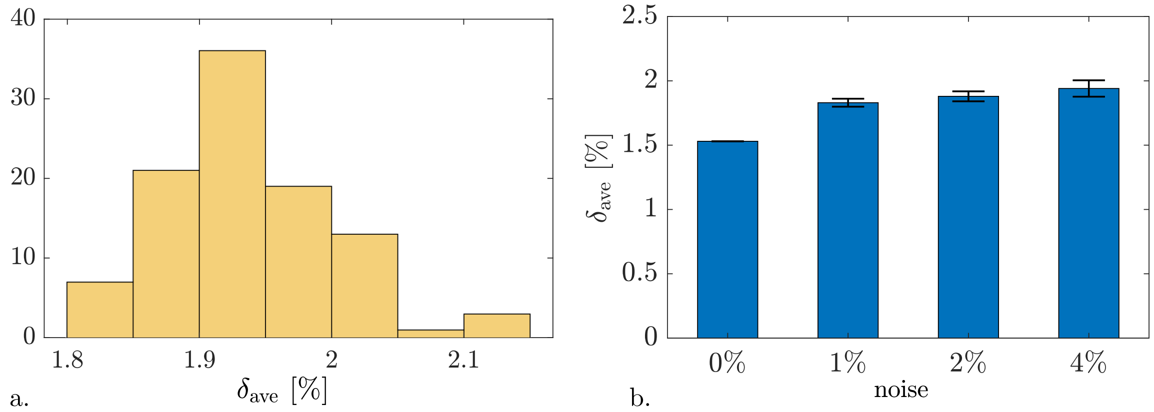

Figure 9: Uniaxial tension: a. histogram of δ_{ave} for 100 runs of Case 1.11; b. error δ_{ave} with its standard deviation for 0% (Case 1.2), 1% (Case 1.6), 2% (Case 1.9) and 4% (Case 1.11) noise.

The mean error and its standard deviation for Cases 1.2, 1.6, 1.9 and 1.11 (0%, 1%, 2% and 4% noise, respectively) are compared in Fig. 9b. No significant difference in the mean of error δ_{ave} is observed for 1%–4% noise. This indicates that, as long as a sufficiently large experimental dataset is used, the mean error is insensitive to noise.
Although the available amount of data makes the problem determined even for a larger number of unknowns, further material discretization with a high noise level can lead to oscillations in solution $\mathbf{q}$ due to *overfitting*, as the comparison between Case 1.11 and Case 1.12 shows. In the latter case the error is much larger, even though the material mesh has been refined. Filtering techniques, known from topology and shape optimization (Sigmund and Petersson, 1998; Bletzinger, 2014), can be applied to deal with the overfitting phenomenon. In this sense, a lower number of material unknowns acts like an inherent filter. This shows that, in order to bring the mean reconstruction error below 2%, at least $n_{\text{el}} = 16 \times 16$ analysis elements, $\bar{n}_{\text{el}} = 8 \times 8$ material reconstruction elements, $n_{\text{exp}}/n_{\text{ll}} = 514 \times 514$ and $n_{\text{ll}} = 2$ need to be used in the presence of 4% noise.
In all cases, the solution of (49) was found in 9–13 iterations. The Jacobian based on the analytical sensitivities (see App. A) provides a tremendous speed-up over numerical (finite-difference based) Jacobians in case of a large number of unknowns: for Case 1.12 the speed-up is about 32.8.[8]

---

[8] For forward finite differences, the cost of one iteration is n_{var} forward problem evaluations, while for the analytic Jacobian only one forward evaluation per iteration is needed. However, building the Jacobian from (79) and (80) involves solving (85) – a system of n_{var} equations.

5.2 Pure bending

The second example, illustrated in Fig. 10a, considers pure unaxial bending of a thin strip, which allows to study the isolated material reconstruction of bending stiffness $c = c(X)$. Two different distributions are examined – a gradual variation in Sec. 5.2.1 and a discontinuous variation in Sec. 5.2.2. The strip has dimension $L_x \times L_y = 4L \times L$. Edge $X = 0$ is fully fixed, while edge $X = 4L$ is only fixed in Z direction (slider support). Both edges are subjected to the distributed bending moment $M_y = 0.5 \cdot 10^{-4}\ FL/L$, where F and L are force and length scales that remain unspecified. Since geometry, load and material only vary along X, but not along Y, the mesh refinement along X is the only relevant discretization parameter in this example.

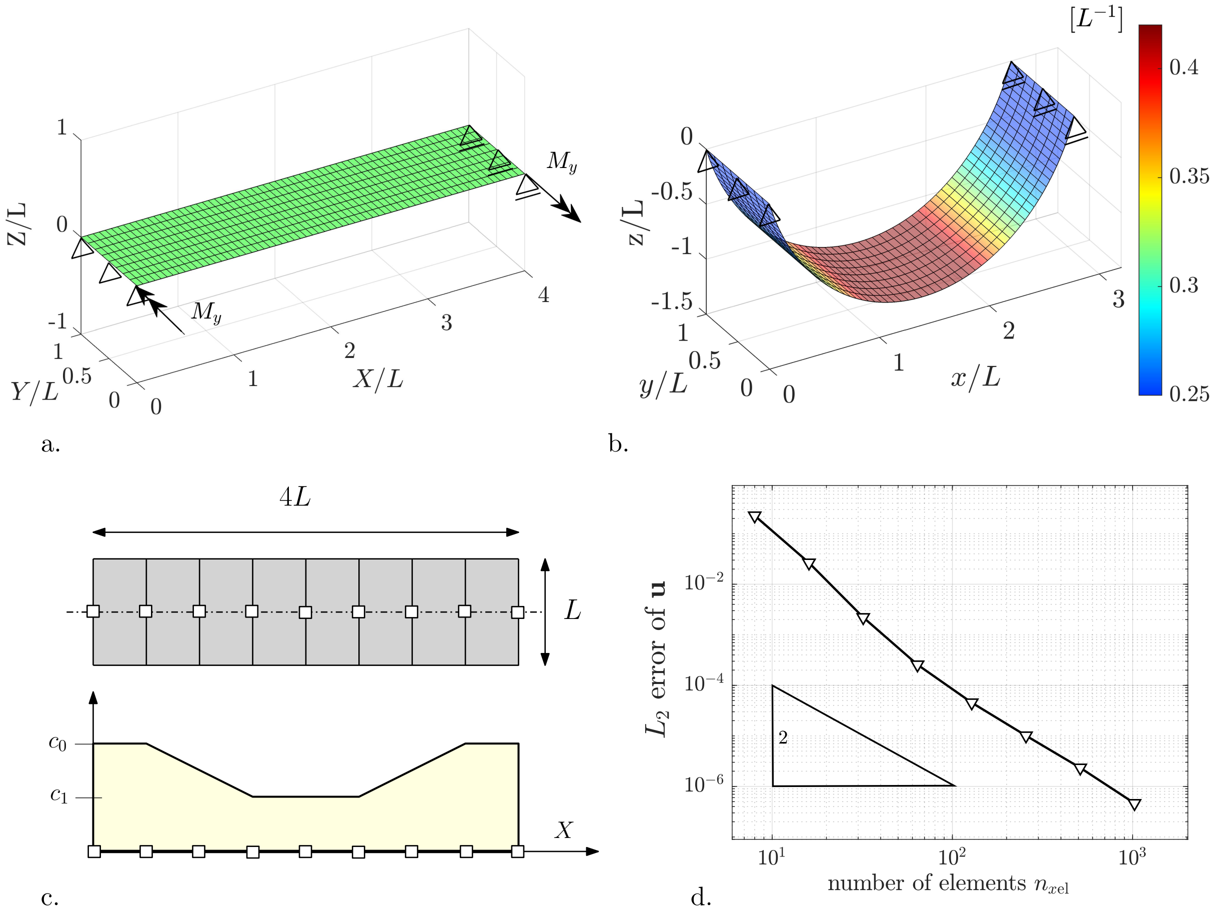

a.

b.

c.

d.

Figure 10: Pure bending (gradual distribution): a. undeformed configuration and boundary conditions; b. deformed configuration colored by the mean curvature, ranging between $0.25/L$ and $0.42/L$; c. material mesh with reference bending stiffness distribution; d. FE convergence of the discrete L_2 error $\|\mathbf{u}_{\text{exact}} - \mathbf{u}_{\text{FE}}\|/\|\mathbf{u}_{\text{exact}}\|$ w.r.t. the refined 'exact' FE solution for $n_{xel} = 4096$ elements.

5.2.1 Gradual material distribution

First, the chosen reference bending stiffness is gradually varying in X- direction by the piecewise linear function

$$c(X) = \begin{cases} c_0 & \text{for} \quad X \leq 0.5L \vee X \geq 3.5L, \\ (c_1 - c_0) \cdot (X/L - 0.5) + c_0 & \text{for} \quad 0.5L < X < 1.5L, \\ c_1 & \text{for} \quad 1.5L \leq X \leq 2.5L, \\ (c_0 - c_1) \cdot (X/L - 2.5) + c_1 & \text{for} \quad 2.5L < X < 3.5L, \end{cases} \tag{67}$$

with $c_0 = 1.0\cdot 10^{-3} FL$ and $c_1 = 0.6\, c_0$, shown in Fig. 10c. This material distribution is captured exactly by $\bar{n}_{x\mathrm{el}} = 8$ material elements ($n_{\mathrm{var}} = \bar{n}_{x\mathrm{no}} = 9$ material nodes), which will be used for all cases studied here. The shear modulus, which does not affect pure bending, but is required for the well-posedness of the FE model, is chosen as $\mu = F/L$ and considered known ($\bar{d} = 1$). This example is not a pure Dirichlet problem, as a bending moment is applied, and so reactions forces are not needed in f. Based on the separate convergence study shown in Fig. 10d, $n_{x\mathrm{el}} = 64$ FE (along the x- direction) are chosen as the analysis mesh for the subsequent inverse analysis. Experiment-like reference results are generated from four load levels (at 25, 50, 75, 100 [%] load) using a fine analysis mesh ($n_{x\mathrm{el}} = 4096$). Objective minimization is conducted with the bounds $c_{\min} = 0.4\, c_0$ and $c_{\max} = 5.0\, c_0$. The initial estimate for the minimization is a vector of random numbers from the range $[c_{\min}, c_{\max}]$.

The results for different noise levels are presented in Tab. 2 and Fig. 11 using the same error definition as in Sec. 5.1. Every case was repeated 25 times to show the influence of the random noise distribution. Since material distribution (67) is captured exactly by the material mesh and the combined reconstruction error hence becomes negligible ($\delta_{\mathrm{ave}} = 0.03\%$ for 0% noise in Case 2.1), the isolated influence of noise on the material reconstruction can be studied in this example. As Tab. 2 and Fig. 11 show, a proportional increase of $\delta_{\max}$, δ_{ave} and its standard deviation is observed. In contrast to uniaxial tension, the relation between δ_{ave} and the noise level is nearly linear. It is explainable by the fact that noise applied to both the x- and z- components, as is considered here, also induces membrane deformations, which cannot be eliminated by changing the bending stiffness, i.e. in-plane membrane deformations are insensitive w.r.t. the bending stiffness, as Eq. (58) also shows. This illustrates that noise cannot be contained if it affects

Case	FE $n_{x\mathrm{el}}$	mat. $\bar{n}_{x\mathrm{el}}$	mat. n_{var}	exp. $n_{\mathrm{exp}}/n_{\mathrm{ll}}$	load n_{ll}	noise [%]	$\delta_{\max}$ [%]	δ_{ave} [%]
2.1	64	8	9	4098	1	0	0.076	0.029
2.2	64	8	9	4098	4	1	1.31 ± 0.68	0.49 ± 0.25
2.3	64	8	9	4098	4	2	2.62 ± 1.36	0.98 ± 0.51
2.4	64	8	9	4098	4	4	5.51 ± 2.52	2.26 ± 1.11

Table 2: Pure bending (gradual distribution): Studied inverse analysis cases with their FE mesh, material mesh, design variables, experimental grid resolution, load level, noise levels, and resulting errors $\delta_{\max}$ and δ_{ave}. 25 repetitions were used for the statistical analysis of Cases 2.2–2.4. Fig. 11 shows a graphical representation of δ_{ave} for the four cases.

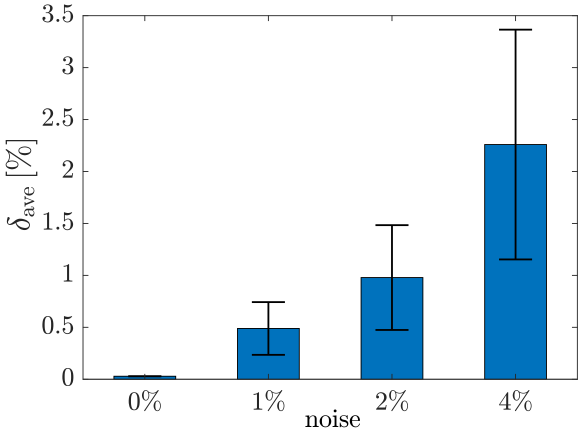

Figure 11: Pure bending (gradual distribution): Mean error and standard deviation of δ_{ave} for noise levels 0%–4%.

material parameters that are not part of $\mathbf{q}$.
The solution of (49) was found in 20–24 iterations for all cases.

5.2.2 Discontinuous material distribution

Second, the more challenging material distribution

$$c(X) = \begin{cases} c_0 & \text{for} \quad X \leq 2L, \\ 25(c_1 - c_0) \cdot (X/L - 2) + c_0 & \text{for} \quad 2L < X < 2.04L, \\ c_1 & \text{for} \quad 2.04L \leq X \leq 4L, \end{cases} \tag{68}$$

is considered with $c_0 = 2.0 \cdot 10^{-3} FL$ and $c_1 = c_0/2$, see Fig. 12c. This distribution has a sharp jump characterized by the relative length scale 1/100 (w.r.t. the strip length $4L$) and results in the discontinuous curvature shown in Fig. 12d. Shear stiffness μ is again kept constant at $\mu = F/L$. Experiment-like reference results are generated from four load levels (at 25, 50, 75, 100 [%] load) using a fine mesh ($n_{x\mathrm{el}} = 4096$). Noise is not applied in order to isolate the influence of the discontinuity. A uniform material mesh with $\bar{n}_{x\mathrm{el}} = 100$ elements of length $0.04L$ is used (Fig. 12a), as it captures the material distribution exactly, and hence allows to also eliminate the influence of material mesh errors. Tab. 3 shows the results of the inverse analysis with the uniform material mesh for three FE analysis meshes (Cases 2.5–2.7). As seen, there are large errors in $\mathbf{q}$ even when 100 FE are used (Case 2.5). These errors are coming from the discontinuity as Fig. 13a shows. Only for 400 FE accurate results for $\mathbf{q}$ are obtained (Case 2.7), see Fig. 13b.

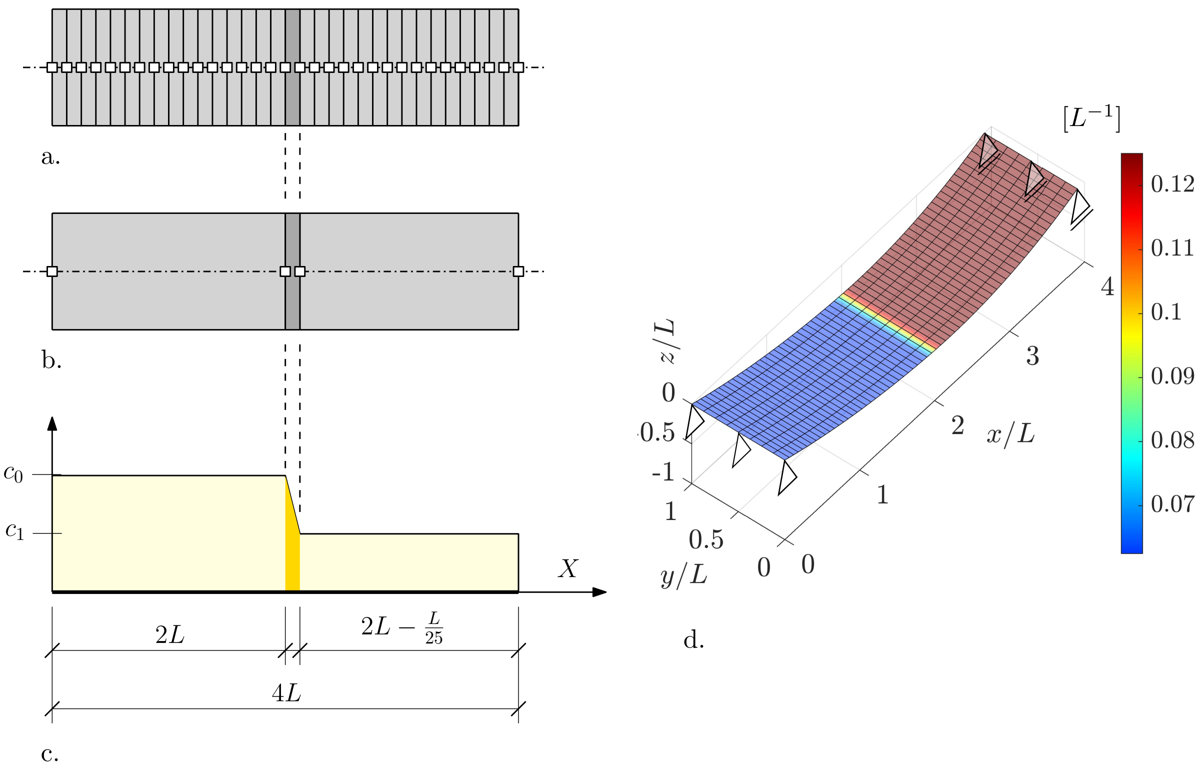

Figure 12: Pure bending (discontinuous distribution): uniform (a.) and adapted (b.) material mesh with reference bending stiffness distribution (c.); d. deformed configuration colored by the mean curvature, ranging between $0.062/L$ and $0.125/L$.

Case	FE n_{xel}	mat. $\bar{n}_{\mathrm{xel}}$	mat. n_{var}	exp. $n_{\mathrm{exp}}/n_{\mathrm{ll}}$	load n_{ll}	noise [%]	δ_{max} [%]	δ_{ave} [%]
2.5	100	100	101	4098	4	0	13.03	1.52
2.6	200	100	101	4098	4	0	3.48	0.093
2.7	400	100	101	4098	4	0	0.76	0.021
2.8	100	3	4	4098	4	0	0.12	0.089

Table 3: Pure bending (discontinuous distribution): Studied inverse analysis cases with their FE mesh, material mesh, design variables, experimental grid resolution, load levels, noise level, and resulting errors δ_{max} and δ_{ave}.

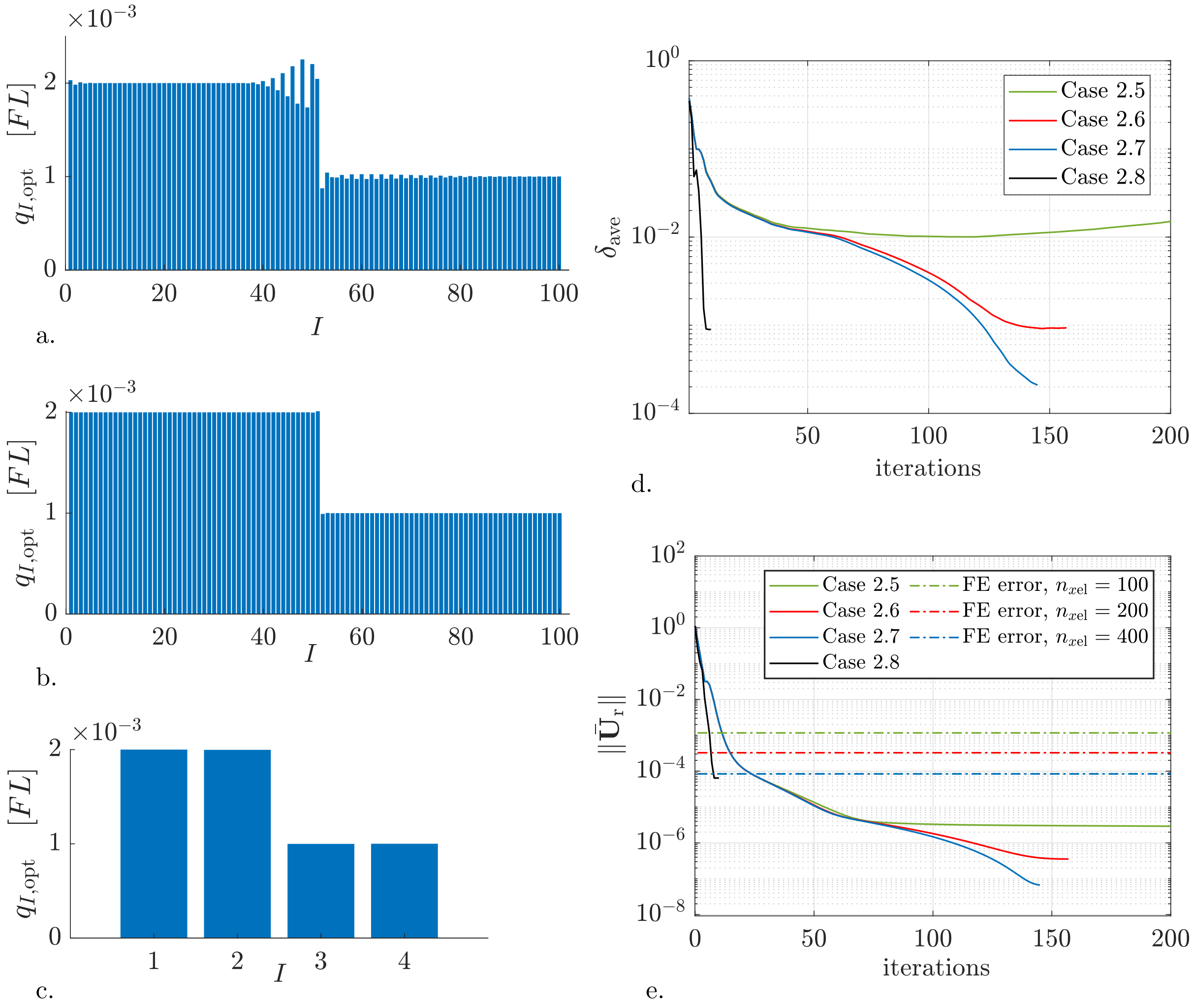

Figure 13: Pure bending (discontinuous distribution): a. Case 2.5 (uniform mesh); b. Case 2.7 (uniform mesh); c. Case 2.8 (adapted mesh); d. evolution of reconstruction error δ_{ave}; e. objective evolution.

The evolution of δ_{ave} is shown in Fig. 13d. The elimination of the error in $\mathbf{q}$ is only possible for a high number of FE and inverse iteration steps. Thus, the proposed method is able to reconstruct discontinuous material distributions, but at the cost of efficiency. Dense FE meshes are needed, since otherwise the FE error in $\mathbf{U}$ overshadows the differences in $\mathbf{U}$ coming from $\mathbf{q}$, making an accurate reconstruction of $\mathbf{q}$ impossible.

The material distribution in (68) suggests an obvious alternative to uniform material meshes: Suppose an adapted material mesh is available, such as the 3-element mesh shown in Fig. 12b.

In this case (denoted 2.8 in Tab. 3), the material can be accurately reconstructed within few iterations even for a comparably coarse analysis mesh, as Fig. 13c–e show. Interestingly, the displacement residual $\|\bar{\mathbf{U}}_\mathrm{r}\|$ is not the lowest for Case 2.8, even though the material error δ_ave is, as Fig. 13d & e show. This illustrates the problem of overfitting: Decreasing $\|\bar{\mathbf{U}}_\mathrm{r}\|$ beyond the FE error tends to wrongly fit the material parameters, which is especially problematic for a high number of design variables.
These results demonstrate that the proposed method, in conjunction with adapted mesh refinement, has the potential to speed-up simulations tremendously, while avoiding overfitting at the same time.

5.3 Sheet inflation

The third example studies the inflation of a square sheet, which induces coupled biaxial membrane and bending deformations and thus tests the capability to simultaneously reconstruct the $\bar{d} = 2$ unknown fields $\mu(\boldsymbol{X})$ and $c(\boldsymbol{X})$. The initially flat sheet with dimension $L_x \times L_y = L \times L$ is pinned on all boundaries and exposed to the uniform pressure $p = 0.5\,FL^2$ prescribed over its entire surface (Fig. 14a, 14b). The material is defined with heterogeneous bending and membrane stiffness according to distribution (65) (see Fig. 6a) with $\mu_0 = FL\,, \Delta\mu_1 = \mu_0$, $c_0 = 0.001FL$ and $\Delta c_1 = c_0$. 8×8 material elements are chosen to reconstruct the material distribution based on the results from the uniaxial tension example, where the same distribution was used. This

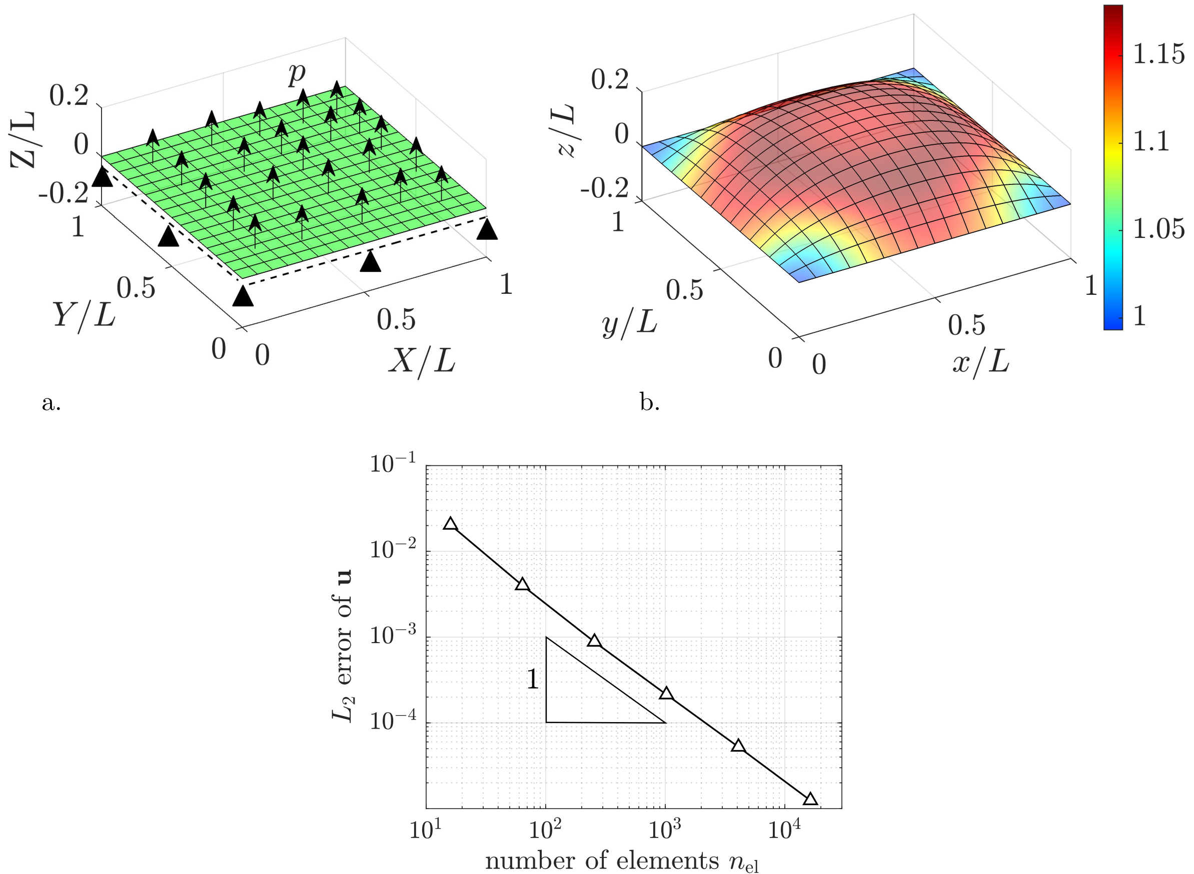

a.
b.
c.

Figure 14: Sheet inflation: a. undeformed configuration and boundary conditions; b. deformed configuration colored by the surface stretch J, ranging between 1.0 and 1.18; c. convergence of the discrete L_2 error $\|\mathbf{u}_\mathrm{exact} - \mathbf{u}_\mathrm{FE}\|/\|\mathbf{u}_\mathrm{exact}\|$, where $\mathbf{u}_\mathrm{exact}$ is the FE solution for $n_\mathrm{el} = 512 \times 512$ elements.

example is not a pure Dirichlet problem, and so no reaction force are required in f. Due to symmetry, only ≈1/4 of the material nodes ($\bar{n}_{\mathrm{no}} = 25$) are treated as design variables (see Fig. 6b). Objective minimization is performed with the lower bounds $c_{\min} = 0.4\,c_0$, $\mu_{\min} = 0.1\,\mu_0$ and the upper bounds $c_{\max} = 5.0\,c_0$, $\mu_{\max} = 5.0\,\mu_0$. The initial estimate for the reconstruction algorithm is a vector of random numbers from the range $[c_{\min}, c_{\max}]$ and $[\mu_{\min}, \mu_{\max}]$. The results of the identification are collected in Tab. 4 and illustrated for selected cases in Figs. 15 and 16.

Case	FE n_{el}	mat. $\bar{n}_{\mathrm{el}}$	mat. n_{var}	$q(\boldsymbol{X})$	exp. $n_{\mathrm{exp}}/n_{\mathrm{ll}}$	load $\mathrm{n_{ll}}$	noise [%]	$\delta_{\max}$ [%]	δ_{ave} [%]
3.1	16×16	8×8	25	μ	130^2	1	0	4.99	1.53
3.2	16×16	8×8	25	c	130^2	1	0	4.75	1.96
3.3	32×32	8×8	50	μ	130^2	1	0	4.19	1.86
				c				24.99	8.58
3.4	32×32	8×8	50	μ	130^2	4	0	5.04	1.98
				c				5.42	2.42
3.5	32×32	8×8	50	μ	514^2	4	1	5.08 ± 0.036	1.99 ± 0.045
				c				5.97 ± 0.33	2.41 ± 0.065
3.6	32×32	8×8	50	μ	514^2	4	2	5.28 ± 0.63	2.01 ± 0.068
				c				6.75 ± 0.71	2.45 ± 0.098
3.7	32×32	8×8	50	μ	514^2	4	4	5.71 ± 1.36	2.02 ± 0.11
				c				8.99 ± 1.65	2.81 ± 0.31

Table 4: Sheet inflation: Studied inverse analysis cases with their FE mesh, material mesh, design variables, experimental grid resolution, load levels, noise level, and resulting errors $\delta_{\max}$ and δ_{ave}. 25 repetitions were used for the statistical analysis of Cases 3.5–3.7. The four highlighted cases are compared in Fig. 16.

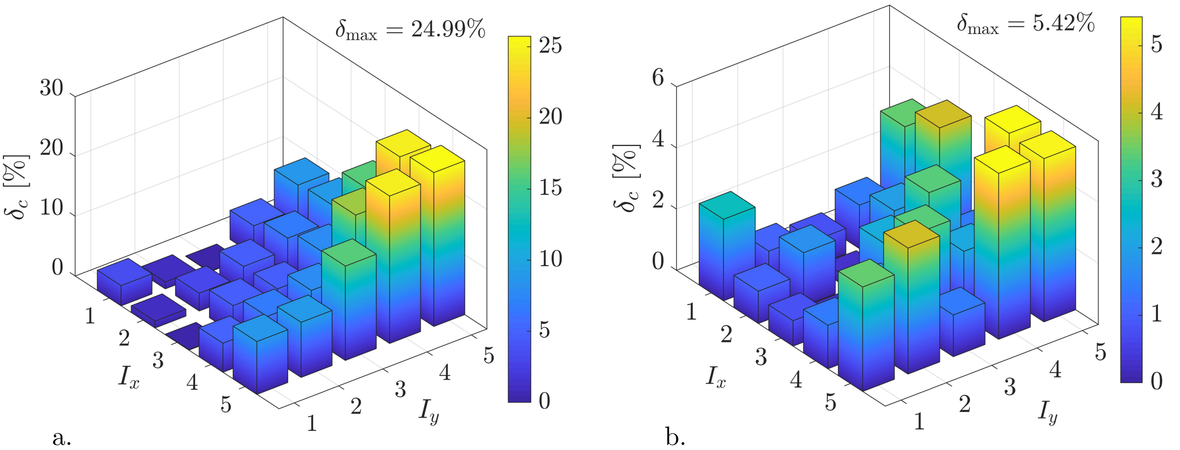

a. b.

Figure 15: Sheet inflation: Comparison of nodal error δ_I of the bending stiffness c for: a. Case 3.3, b. Case 3.4.

In Cases 3.1 and 3.2 only one parameter is identified, while the remaining parameter is assumed given by distribution Eq. (65). The maximum and average errors are similar to Case 1.2 in Tab. 1, which shows a predictable performance of the optimization when the two material

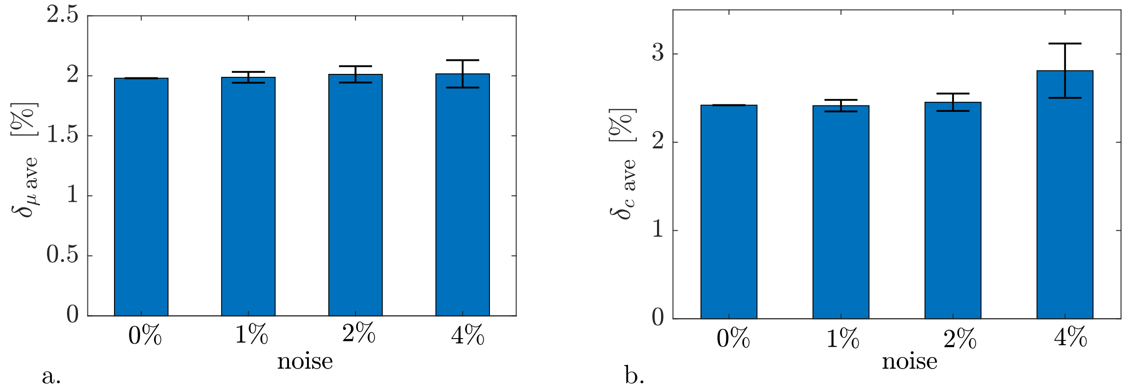

Figure 16: Sheet inflation: Comparison of the mean and standard deviation of error δ_{ave} for 0% (Case 3.4), 1% (Case 3.5), 2% (Case 3.6) and 4% (Case 3.7) noise for: a. shear modulus μ, b. bending stiffness c.

parameters are uncoupled. Problems with coupled membrane and bending behavior exhibit additional challenges compared to uncoupled problems such as those in Sec. 5.1 & 5.2. One, are the different units of membrane stiffness μ and bending stiffness c. Working with normalized quantities, as is done here, alleviates this problem. Another challenge are the different sensitivities of parameters μ and c. As a remedy (not considered here) different weights for parameters μ and c could be considered in the objective function (49). However, this can still not be expected to fully solve the problem, as the two sensitivities dependent differently on location and deformation. The bending sensitivity, for instance, can be expected to play a larger role at the boundary than in the center of the sheet. As is known from nonlinear plate and shell theory, the early load stages engage bending more than membrane deformations, i.e. the bending sensitivity (59) can be expected to be more dominant at small loads, while the membrane sensitivity (58) can be expected to be more influential at high loads. Therefore the bending stiffness cannot be expected to be reconstructed very well, if only the last load step is taken into account. This can be seen by comparing Cases 3.3 and 3.4 as is done in Fig. 15. As seen, using four load steps (at $25, 50, 75, 100$ [%] load) reduces the error in δ_c significantly.

The parameters n_{el}, $\bar{n}_{\text{el}}$ and n_{ll} of case 3.4 are further used in Cases 3.5–3.7 to study the influence of noise. Each case is repeated 25 times and the influence of the noise on the error δ_{ave} for both parameters is shown in Fig. 16. Ultimately, for Case 3.7 (4% noise), errors δ_{max} and δ_{ave} were found at $8.99 \pm 1.65\%$ (mean ± standard deviation) and $2.81 \pm 0.31\%$, respectively, for bending stiffness c, and $5.71 \pm 1.36\%$ and $2.02 \pm 0.11\%$ for shear modulus μ. The comparison with Case 3.4, where no noise was applied, shows good performance of the algorithm in the presence of increasing noise. The results indicate that the mean error (but not its variation) is independent of the noise, as long as the experimental dataset is sufficiently large, which does seem to be the case for c in Case 3.7. This behavior can be expected for noise that is symmetrically distributed around zero, as is considered here. If the noise is distributed differently, it can be expected to affect the mean error also.

Throughout all cases, the inverse solution was found after 9–11 iterations.

5.4 Abdominal wall under pressure loading

The last example considers the pressurization of the human abdominal wall in order to identify its Young's modulus and thickness distribution ($\bar{d} = 2$). A single-patch NURBS discretization is used (Borzeszkowski et al., 2020), which is based on the geometry model of Lubowiecka et al. (2017) and the measurement methodology of Szymczak et al. (2012). The initially curved surface is pinned on all boundaries and exposed to the uniform pressure $p = 1.6\,\text{kPa}$, which corresponds to the intra-abdominal pressure level (12 mmHg) in laparoscopic surgeries (Song et al., 2006; Pachera et al., 2016), see Fig. 17a and 17b. 168 × 168 finite elements are used to

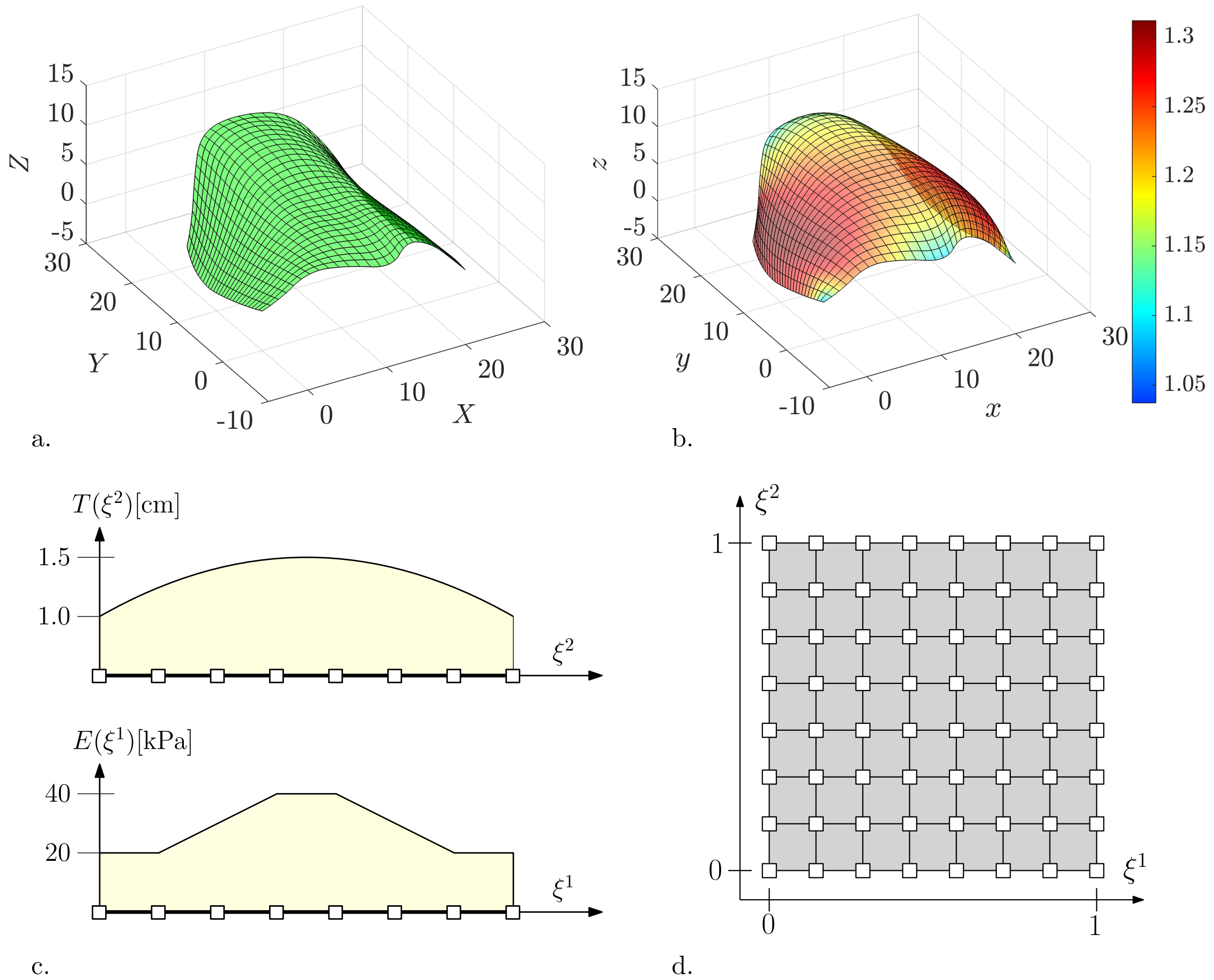

Figure 17: Abdominal wall: a. undeformed configuration; b. deformed configuration colored by the surface stretch J, ranging between 1.04 and 1.31; c. reference distribution for Young's modulus E and thickness T; d. material mesh.

generate experiment-like results for the deformation field, incorporating four load levels (at 25, 50, 75, 100 [%] load). For the sake of demonstration, an analytic reference distribution of the material is chosen. It is defined in the domain $\boldsymbol{\xi}$ and mapped on the surface $\mathcal{S}_0$. The Koiter material model (Sec. 2.3.2) is considered with varying Young's modulus in $\xi^1 \mapsto X$ direction

$$E(\xi^1) = \begin{cases} E_1 & \text{for} \quad \xi^1 \leq \frac{1}{7} \vee \xi^1 \geq \frac{6}{7}, \\ E_1 + \frac{1}{2}(E_2 - E_1) \cdot (7\xi^1 - 1) & \text{for} \quad \frac{1}{7} < \xi^1 < \frac{3}{7}, \\ E_2 & \text{for} \quad \frac{3}{7} \leq \xi^1 \leq \frac{4}{7}, \\ E_2 - \frac{1}{2}(E_2 - E_1) \cdot (7\xi^1 - 4) & \text{for} \quad \frac{4}{7} < \xi^1 < \frac{6}{7}, \end{cases} \qquad \xi^1 \in [0,1], \tag{69}$$

and varying thickness in the $\xi^2 \mapsto Y$ direction

$$T(\xi^2) = T_2 - (T_2 - T_1)(2\,\xi^2 - 1)^2\,, \quad \xi^2 \in [0,1], \tag{70}$$

with $T_1 = 1\,\text{cm}$, $T_2 = 1.5\,\text{cm}$, $E_1 = 20\,\text{kPa}$, $E_2 = 40\,\text{kPa}$, see Fig. 17c. The Koiter parameters μ and Λ are then calculated from (26). 7 × 7 bilinear material elements are used to capture the material distribution (Fig. 17d). Objective minimization is performed with the lower bounds [5 kPa, 0.5 cm] and the upper bounds [100 kPa, 5.0 cm]. The constant initial estimates $E = 6\,\text{kPa}$ and $T = 4\,\text{cm}$ are considered. Results, for different FE meshes and noise level, are collected in Tab. 5 and illustrated in Fig. 18.

Case	FE n_{el}	mat. $\bar{n}_{\text{el}}$	mat. n_{var}	$q(\boldsymbol{X})$	exp. $n_{\text{exp}}/n_{\text{ll}}$	load n_{ll}	noise [%]	δ_{max} [%]	δ_{ave} [%]
4.1	28×28	7×7	128	E	170^2	4	0	53.07 (10.59)	3.68 (2.18)
				T				43.01 (10.49)	3.19 (1.97)
4.2	56×56	7×7	128	E	170^2	4	0	34.79 (4.83)	1.69 (0.72)
				T				29.19 (4.79)	1.49 (0.66)
4.3	56×56	7×7	128	E	170^2	4	1	34.74 ± 0.19	1.74 ± 0.029
				T				29.17 ± 0.19	1.53 ± 0.02
4.4	56×56	7×7	128	E	170^2	4	2	34.78 ± 0.41	1.83 ± 0.054
				T				29.17 ± 0.31	1.61 ± 0.05
4.5	56×56	7×7	128	E	170^2	4	4	34.6 ± 0.85	2.1 ± 0.15
				T				29.15 ± 0.79	1.87 ± 0.13

Table 5: Abdominal wall: Studied inverse analysis cases with their FE mesh, material mesh, design variables, experimental grid resolution, load levels, noise level, and resulting errors δ_{max} and δ_{ave}. The values in brackets show the errors excluding the upper corner values. 25 repetitions were used for the statistical analysis of Cases 4.3–4.5.

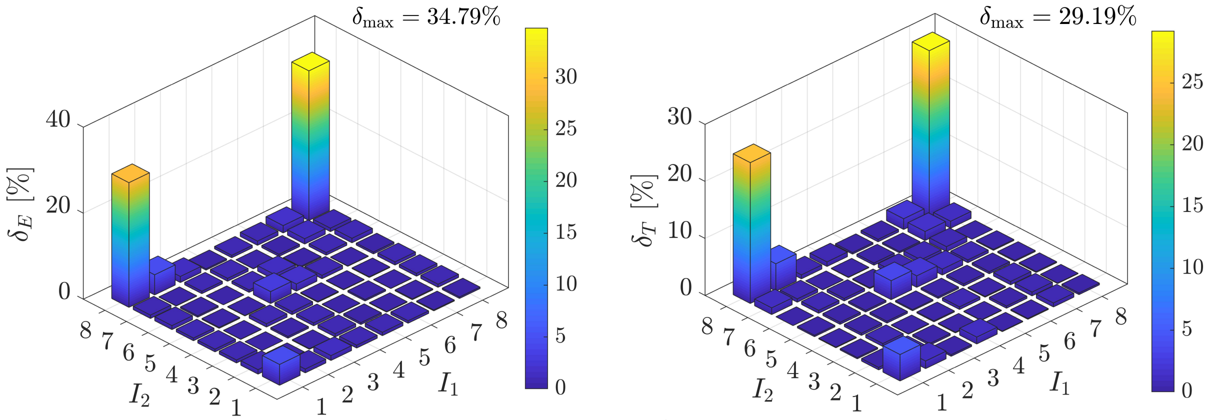

a.

b.

Figure 18: Abdominal wall: Case 4.2, nodal error δ_I of: a. Young's modulus E; b. thickness T.

High accuracy is met, except at the upper corner nodes, where high errors δ_{max} and δ_{ave} are observed (see Fig. 18). FE refinement decreases the errors, as Cases 4.1 and 4.2 show, but corner errors remain still high. The poor corner accuracy indicates that the pressurization test is insensitive to the corner parameters of the considered geometry model, resulting in the inability to reconstruct those values accurately. The incorporation of additional tests, as well as the consideration of different geometry models, are expected to eliminate corner inaccuracies. The statistical analysis in Cases 4.3–4.5 shows that noise has a minor influence on the material reconstruction.

6 Conclusions

This work presents an inverse material identification procedure based on an isogeometric shell formulation and the FEMU. The procedure is very general and able to identify heterogeneous material distributions for challenging nonlinear inverse problems in the presence of measurement error. The theoretical framework accounts for large deformations and is based on a general material law definition with independent membrane and bending contributions that is suitable to model a large range of materials. The discretization of the governing equations and heterogeneous material parameter fields use efficient isogeometric shell elements and bilinear Lagrange elements, respectively. The former provide high continuity to accurately and efficiently describe deforming shells, while the latter is a good compromise for various materials that can be expected to contain both discontinuous and graded material properties. Moreover, the material discretization is independent from the analysis mesh, which allows to efficiently and accurately capture material discontinuities using adapted meshes, as they reduce the number of design variables and avoid overfitting. The minimization of the resulting least-squares objective is conducted with a trust region algorithm in-build to MATLAB. Using the analytical Jacobians results in a major speed-up compared to using finite difference approximations of the Jacobians. Various possible approximation errors and their influence on the inverse algorithm are discussed. Several numerical examples demonstrate the ability of the algorithm to contain all these errors. In order to mimic measurement errors in experiments, experiment-like data is produced by a highly-resolved forward problem with given analytical reference material distribution and the addition of random noise.

The biggest benefit of the proposed identification framework is that its building blocks can be easily substituted or extended. The trust-region algorithm can be replaced by a different optimization scheme to increase efficiency, assure global convergence and account for uncertainties. Another extension is the consideration of more sophisticated constitutive laws. The membrane and bending energy split favors combining and studying different material models, while the proposed discretization allows for local mesh refinement that can accurately account for possible material variations and discontinuities. To automate this process, adaptive meshing techniques need to be developed, which is planned for future work. Also, we plan to extend the abdominal wall study in Sec. 5.4 to the material identification of human abdominal wall tissue based on *in vivo* measurements as reported for example in Lubowiecka et al. (2022). Furthermore, thick and composite shell formulations with various constraints (contact, volume, area) can be used. Although we focus on material identification, additional parameters can be used as design variables. An important example relevant to experimental material reconstruction is the stiffness of the specimen fixations.

Acknowledgements

We thank Dr. Thang Duong and Karsten Paul for their comments and support. This work has been partially supported by the National Science Centre (Poland) under Grant No. 2017/27/B/ST8/02518. Calculations have been carried out at the Academic Computing Centre in Gdańsk.

A Gradient and Hessian of the objective function

Introducing the residual

$$\bar{\mathbf{U}}_{\mathrm{r}}(\mathbf{q}) := \bar{\mathbf{U}}_{\mathrm{exp}} - \bar{\mathbf{U}}_{\mathrm{FE}}(\mathbf{q}), \tag{71}$$

with

$$\bar{\mathbf{U}}_{\text{exp}} := \begin{bmatrix} \mathbf{U}_{\text{exp}}/\|\mathbf{U}_{\text{exp}}\| \\ \mathbf{R}_{\text{exp}}/\|\mathbf{R}_{\text{exp}}\| \end{bmatrix}, \qquad \bar{\mathbf{U}}_{\text{FE}}(\mathbf{q}) := \begin{bmatrix} \mathbf{U}_{\text{FE}}(\mathbf{q})/\|\mathbf{U}_{\text{exp}}\| \\ \mathbf{R}_{\text{FE}}(\mathbf{q})/\|\mathbf{R}_{\text{exp}}\| \end{bmatrix} \tag{72}$$

the objective function of (49) simply becomes

$$f = \frac{1}{2}\bar{\mathbf{U}}_{\text{r}}^{\text{T}}\bar{\mathbf{U}}_{\text{r}}. \tag{73}$$

The gradient of $f(\mathbf{q})$ w.r.t to the design variable vector $\mathbf{q}$ is then given by

$$\mathbf{g}(\mathbf{q}) = \frac{\partial f(\mathbf{q})}{\partial \mathbf{q}} = \mathbf{J}(\mathbf{q})^{\text{T}}\bar{\mathbf{U}}_{\text{r}}(\mathbf{q}) \ . \tag{74}$$

where

$$\mathbf{J}(\mathbf{q}) = \frac{\partial \bar{\mathbf{U}}_{\text{r}}(\mathbf{q})}{\partial \mathbf{q}} = \begin{bmatrix} \mathbf{J}_{\text{U}} \\ \mathbf{J}_{\text{R}} \end{bmatrix}, \tag{75}$$

is the *Jacobian* of the residual that contains the blocks

$$\mathbf{J}_{\text{U}} = -\frac{1}{\|\mathbf{U}_{\text{exp}}\|}\frac{\partial \mathbf{U}_{\text{FE}}(\mathbf{q})}{\partial \mathbf{q}}, \tag{76}$$

and

$$\mathbf{J}_{\text{R}} = -\frac{1}{\|\mathbf{R}_{\text{exp}}\|}\frac{\partial \mathbf{R}_{\text{FE}}(\mathbf{q})}{\partial \mathbf{q}}. \tag{77}$$

The *Hessian* is the matrix of second derivatives of $f(\mathbf{q})$, which now becomes (e.g. see Hansen et al. (2013) for further details)

$$\mathbf{H}(\mathbf{q}) = \frac{\partial^2 f(\mathbf{q})}{\partial \mathbf{q}^2} = \mathbf{J}^{\text{T}}\mathbf{J} + \bar{\mathbf{U}}_{\text{r}}^{\text{T}}\frac{\partial^2 \bar{\mathbf{U}}_{\text{r}}}{\partial \mathbf{q}^2}. \tag{78}$$

Remark 3: One of the benefits of the least-squares form is that the first term in Eq. (78) can be already computed with the given Jacobian. Moreover, the second term is often neglected due to the residual $\bar{\mathbf{U}}_{\text{r}}$ approaching zero near the solution. This approximation is popular in various *trust region* methods, as it allows for an evaluation of the Hessian matrix without extra computation of the second derivative of $\bar{\mathbf{U}}_{\text{r}}$.

In order to calculate the Jacobian in (76), we first need to expand

$$\frac{\partial \mathbf{U}_{\text{FE}}}{\partial \mathbf{q}} = \frac{\partial \mathbf{U}_{\text{FE}}}{\partial \mathbf{u}}\frac{\partial \mathbf{u}}{\partial \mathbf{q}}, \tag{79}$$

where $\mathbf{u}$ is the stacked vector of all n_{no} nodal displacements (45), and $\partial\mathbf{U}_{\text{FE}}/\partial\mathbf{u}$ is assembled from the n_{el} elemental contributions

$$\frac{\partial \mathbf{U}_{\text{FE}}}{\partial \mathbf{u}^e} = \begin{bmatrix} \mathbf{N}^e\big(\boldsymbol{x}_1^{\text{exp}}\big) \\ \mathbf{N}^e\big(\boldsymbol{x}_2^{\text{exp}}\big) \\ \vdots \\ \mathbf{N}^e\big(\boldsymbol{x}_{n_{\text{exp}}}^{\text{exp}}\big) \end{bmatrix}, \qquad e = 1, \dots, n_{\text{el}} \tag{80}$$

that follow directly from (52) and (53). Further, $\partial\mathbf{u}/\partial\mathbf{q}$ is required in (79). For the Dirichlet boundary nodes, $\mathbf{u}$ is prescribed independently of $\mathbf{q}$ and hence $\partial\mathbf{u}/\partial\mathbf{q}$ is zero. For the free nodes, $\partial\mathbf{u}/\partial\mathbf{q}$ follows from the FE element equilibrium equation (44), which depends on $\mathbf{q}$ as follows

$$\mathbf{f}\big(\mathbf{u}(\mathbf{q}), \mathbf{q}\big) = \mathbf{f}_{\text{int}}\big(\mathbf{u}(\mathbf{q}), \mathbf{q}\big) - \mathbf{f}_{\text{ext}}\big(\mathbf{u}\big) = \mathbf{0} \ . \tag{81}$$

Differentiating Eq. (81) w.r.t. the design variable vector $\mathbf{q}$ then gives

$$\frac{\text{d}\mathbf{f}}{\text{d}\mathbf{q}} = \frac{\partial \mathbf{f}_{\text{int}}}{\partial \mathbf{q}} + \frac{\partial \mathbf{f}_{\text{int}}}{\partial \mathbf{u}}\frac{\partial \mathbf{u}}{\partial \mathbf{q}} - \frac{\partial \mathbf{f}_{\text{ext}}}{\partial \mathbf{q}} - \frac{\partial \mathbf{f}_{\text{ext}}}{\partial \mathbf{u}}\frac{\partial \mathbf{u}}{\partial \mathbf{q}} = \mathbf{0}\,. \tag{82}$$

Rewriting this equation gives

$$\frac{\partial \mathbf{u}}{\partial \mathbf{q}} = -\left(\frac{\partial \mathbf{f}_{\text{int}}}{\partial \mathbf{u}} - \frac{\partial \mathbf{f}_{\text{ext}}}{\partial \mathbf{u}}\right)^{-1}\left(\frac{\partial \mathbf{f}_{\text{int}}}{\partial \mathbf{q}} - \frac{\partial \mathbf{f}_{\text{ext}}}{\partial \mathbf{q}}\right). \tag{83}$$

Introducing the tangent stiffness matrix

$$\mathbf{K} = \frac{\partial \mathbf{f}_{\text{int}}}{\partial \mathbf{u}} - \frac{\partial \mathbf{f}_{\text{ext}}}{\partial \mathbf{u}}, \tag{84}$$

and accounting for the fact that the external load vector $\mathbf{f}_{\text{ext}}$ does not depend on $\mathbf{q}$, Eq. (83) can be expressed as

$$\frac{\partial \mathbf{u}}{\partial \mathbf{q}} = -\mathbf{K}^{-1}\frac{\partial \mathbf{f}_{\text{int}}}{\partial \mathbf{q}}, \tag{85}$$

where the $\partial \mathbf{f}_{\text{int}}/\partial \mathbf{q}$ is the global sensitivity matrix $\mathbf{S}$ (analogous to Eq. (56)).
In order to calculate the Jacobian in (77), we note that reaction force $\mathbf{R}_{\text{FE}}$ directly follows from equilibrium at the Dirichlet nodes, given by

$$\mathbf{R}_{\text{FE}} = \mathbf{f}^{\text{b}}_{\text{int}}(\mathbf{u}(\mathbf{q}), \mathbf{q}) - \mathbf{f}^{\text{b}}_{\text{ext}}(\mathbf{u}). \tag{86}$$

Here superscript "b" denotes the boundary forces, that are different from the forces of the free nodes given in (81). From (86) follows

$$\frac{\partial \mathbf{R}_{\text{FE}}}{\partial \mathbf{q}} = \frac{\partial \mathbf{f}^{\text{b}}_{\text{int}}}{\partial \mathbf{q}} + \frac{\partial \mathbf{f}^{\text{b}}_{\text{int}}}{\partial \mathbf{u}}\frac{\partial \mathbf{u}}{\partial \mathbf{q}} - \frac{\partial \mathbf{f}^{\text{b}}_{\text{ext}}}{\partial \mathbf{q}} - \frac{\partial \mathbf{f}^{\text{b}}_{\text{ext}}}{\partial \mathbf{u}}\frac{\partial \mathbf{u}}{\partial \mathbf{q}}. \tag{87}$$

Introducing

$$\mathbf{K}^{\text{b}} := \frac{\partial \mathbf{f}^{\text{b}}_{\text{int}}}{\partial \mathbf{u}} - \frac{\partial \mathbf{f}^{\text{b}}_{\text{ext}}}{\partial \mathbf{u}}, \tag{88}$$

and using (85) and $\partial \mathbf{f}^{\text{b}}_{\text{ext}}/\partial \mathbf{q} = \mathbf{0}$, then gives

$$\frac{\partial \mathbf{R}_{\text{FE}}}{\partial \mathbf{q}} = \mathbf{S}^{\text{b}} - \mathbf{K}^{\text{b}}\frac{\partial \mathbf{u}}{\partial \mathbf{q}}. \tag{89}$$

where

$$\mathbf{S}^{\text{b}} := \frac{\partial \mathbf{f}^{\text{b}}_{\text{int}}}{\partial \mathbf{q}} \tag{90}$$

is the sensitivity at the boundary. With this, all pieces are given to evaluate $\mathbf{g}$ in (74) and $\mathbf{H}$ according to Remark 3.

References

Aernouts, J. and Dirckx, J. J. (2011). Elastic characterization of the gerbil pars flaccida from in situ inflation experiments. *Biomechanics and Modeling in Mechanobiology*, **10**(5):727–741.

Avril, S., Badel, P., and Duprey, A. (2010). Anisotropic and hyperelastic identification of in vitro human arteries from full-field optical measurements. *Journal of Biomechanics*, **43**(15):2978–2985.

Avril, S., Bonnet, M., Bretelle, A.-S., Grédiac, M., Hild, F., Ienny, P., Latourte, F., Lemosse, D., Pagano, S., Pagnacco, E., et al. (2008). Overview of identification methods of mechanical parameters based on full-field measurements. *Experimental Mechanics*, **48**(4):381.

Avril, S., Grédiac, M., and Pierron, F. (2004). Sensitivity of the virtual fields method to noisy data. *Computational Mechanics*, **34**(6):439–452.

Avril, S. and Pierron, F. (2007). General framework for the identification of constitutive parameters from full-field measurements in linear elasticity. *International Journal of Solids and Structures*, **44**(14-15):4978–5002.

Badel, P., Avril, S., Lessner, S., and Sutton, M. (2012). Mechanical identification of layer-specific properties of mouse carotid arteries using 3D-DIC and a hyperelastic anisotropic constitutive model. *Computer Methods in Biomechanics and Biomedical Engineering*, **15**(1):37–48.

Benson, D., Bazilevs, Y., Hsu, M.-C., and Hughes, T. J. R. (2011). A large deformation, rotation-free, isogeometric shell. *Computer Methods in Applied Mechanics and Engineering*, **200**(13-16):1367–1378.

Bersi, M. R., Bellini, C., Di Achille, P., Humphrey, J. D., Genovese, K., and Avril, S. (2016). Novel methodology for characterizing regional variations in the material properties of murine aortas. *Journal of Biomechanical Engineering*, **138**(7):0710051.

Bischoff, J. E., Drexler, E. S., Slifka, A. J., and McCowan, C. N. (2009). Quantifying nonlinear anisotropic elastic material properties of biological tissue by use of membrane inflation. *Computer Methods in Biomechanics and Biomedical Engineering*, **12**(3):353–369.

Bletzinger, K.-U. (2014). A consistent frame for sensitivity filtering and the vertex assigned morphing of optimal shape. *Structural and Multidisciplinary Optimization*, **49**(6):873–895.

Borden, M. J., Scott, M. A., Evans, J. A., and Hughes, T. J. R. (2011). Isogeometric finite element data structures based on Bézier extraction of NURBS. *International Journal for Numerical Methods in Engineering*, **87**(1-5):15–47.

Borzeszkowski, B., Duong, T. X., Sauer, R. A., and Lubowiecka, I. (2020). Isogeometric shell analysis of the human abdominal wall. In Gzik, M., Paszenda, Z., Pietka, E., Tkacz, E., and Milewski, K., editors, *International Scientific Conference Advances in Applied Biomechanics*, pages 11–18. Springer.

Canham, P. B. (1970). The minimum energy of bending as a possible explanation of the biconcave shape of the human red blood cell. *Journal of Theoretical Biology*, **26**(1):61–81.

Ciarlet, P. G. (2005). An introduction to differential geometry with applications to elasticity. *Journal of Elasticity*, **78**(1):1–215.

Coleman, T. F. and Li, Y. (1996). An interior trust region approach for nonlinear minimization subject to bounds. *SIAM Journal on Optimization*, **6**(2):418–445.

Colton, D. L. and Kress, R. (1998). *Inverse Acoustic and Electromagnetic Scattering Theory*, volume **93** of *Applied Mathematical Sciences*. Springer, Cham.

Conn, A. R., Gould, N. I., and Toint, P. L. (2000). *Trust Region Methods*. SIAM.

Davis, F. M., Luo, Y., Avril, S., Duprey, A., and Lu, J. (2015). Pointwise characterization of the elastic properties of planar soft tissues: application to ascending thoracic aneurysms. *Biomechanics and Modeling in Mechanobiology*, **14**(5):967–978.

De Lorenzis, L., Wriggers, P., and Hughes, T. J. R. (2014). Isogeometric contact: a review. *GAMM-Mitteilungen*, **37**(1):85–123.

Dedè, L., Borden, M. J., and Hughes, T. J. (2012). Isogeometric analysis for topology optimization with a phase field model. *Archives of Computational Methods in Engineering*, **19**(3):427–465.

Do, H. V., Lahmer, T., Zhuang, X., Alajlan, N., Nguyen-Xuan, H., and Rabczuk, T. (2019). An isogeometric analysis to identify the full flexoelectric complex material properties based on electrical impedance curve. *Computers & Structures*, **214**:1–14.

Dufour, J.-E., Hild, F., and Roux, S. (2015). Shape, displacement and mechanical properties from isogeometric multiview stereocorrelation. *The Journal of Strain Analysis for Engineering Design*, **50**(7):470–487.

Duong, T. X., Roohbakhshan, F., and Sauer, R. A. (2017). A new rotation-free isogeometric thin shell formulation and a corresponding continuity constraint for patch boundaries. *Computer Methods in Applied Mechanics and Engineering*, **316**:43–83.

Evans, S. (2017). How can we measure the mechanical properties of soft tissues? In Avril, S. and Evans, S., editors, *Material Parameter Identification and Inverse Problems in Soft Tissue Biomechanics*, pages 67–83. Springer.

Farzaneh, S., Trabelsi, O., and Avril, S. (2019a). Inverse identification of local stiffness across ascending thoracic aortic aneurysms. *Biomechanics and Modeling in Mechanobiology*, **18**(1):137–153.

Farzaneh, S., Trabelsi, O., Chavent, B., and Avril, S. (2019b). Identifying local arterial stiffness to assess the risk of rupture of ascending thoracic aortic aneurysms. *Annals of Biomedical Engineering*, **47**(4):1038–1050.

Genovese, K., Casaletto, L., Humphrey, J. D., and Lu, J. (2014). Digital image correlation-based point-wise inverse characterization of heterogeneous material properties of gallbladder in vitro. *Proceedings of the Royal Society A: Mathematical, Physical and Engineering Sciences*, **470**(2167):20140152.

Genovese, K., Lamberti, L., and Pappalettere, C. (2006). Mechanical characterization of hyperelastic materials with fringe projection and optimization techniques. *Optics and Lasers in Engineering*, **44**(5):423–442.

Goenezen, S., Dord, J.-F., Sink, Z., Barbone, P. E., Jiang, J., Hall, T. J., and Oberai, A. A. (2012). Linear and nonlinear elastic modulus imaging: an application to breast cancer diagnosis. *IEEE transactions on Medical Imaging*, **31**(8):1628–1637.

Guo, Y. and Ruess, M. (2015). Weak Dirichlet boundary conditions for trimmed thin isogeometric shells. *Computers & Mathematics with Applications*, **70**(7):1425–1440.

Hansen, P. C., Pereyra, V., and Scherer, G. (2013). *Least Squares Data Fitting with Applications*. JHU Press.

Hughes, T. J. R., Cottrell, J. A., and Bazilevs, Y. (2005). Isogeometric analysis: CAD, finite elements, NURBS, exact geometry and mesh refinement. *Computer Methods in Applied Mechanics and Engineering*, **194**(39-41):4135–4195.

Iding, R. H., Pister, K. S., and Taylor, R. L. (1974). Identification of nonlinear elastic solids by a finite element method. *Computer Methods in Applied Mechanics and Engineering*, **4**(2):121–142.

Kauer, M., Vuskovic, V., Dual, J., Székely, G., and Bajka, M. (2002). Inverse finite element characterization of soft tissues. *Medical Image Analysis*, **6**(3):275–287.

Kavanagh, K. T. and Clough, R. W. (1971). Finite element applications in the characterization of elastic solids. *International Journal of Solids and Structures*, **7**(1):11–23.

Khalil, A. S., Bouma, B. E., and Mofrad, M. R. K. (2006). A combined FEM/genetic algorithm for vascular soft tissue elasticity estimation. *Cardiovascular Engineering*, **6**(3):93–102.

Kiendl, J., Bletzinger, K.-U., Linhard, J., and Wüchner, R. (2009). Isogeometric shell analysis with Kirchhoff–Love elements. *Computer Methods in Applied Mechanics and Engineering*, **198**(49-52):3902–3914.

Kiendl, J., Hsu, M.-C., Wu, M. C., and Reali, A. (2015). Isogeometric Kirchhoff–Love shell formulations for general hyperelastic materials. *Computer Methods in Applied Mechanics and Engineering*, **291**:280–303.

Kiendl, J., Schmidt, R., Wüchner, R., and Bletzinger, K.-U. (2014). Isogeometric shape optimization of shells using semi-analytical sensitivity analysis and sensitivity weighting. *Computer Methods in Applied Mechanics and Engineering*, **274**:148–167.

Kroon, M. (2010a). An efficient method for material characterisation of hyperelastic anisotropic inhomogeneous membranes based on inverse finite-element analysis and an element partition strategy. *Quarterly Journal of Mechanics and Applied Mathematics*, **63**(2):201–225.

Kroon, M. (2010b). A numerical framework for material characterisation of inhomogeneous hyperelastic membranes by inverse analysis. *Journal of Computational and Applied Mathematics*, **234**(2):563–578.

Kroon, M. and Holzapfel, G. A. (2008). Estimation of the distributions of anisotropic, elastic properties and wall stresses of saccular cerebral aneurysms by inverse analysis. *Proceedings of the Royal Society A: Mathematical, Physical and Engineering Sciences*, **464**(2092):807–825.

Kroon, M. and Holzapfel, G. A. (2009). Elastic properties of anisotropic vascular membranes examined by inverse analysis. *Computer Methods in Applied Mechanics and Engineering*, **198**(45):3622–3632.

Kyriacou, S. K., Shah, A. D., and Humphrey, J. D. (1997). Inverse Finite Element Characterization of Nonlinear Hyperelastic Membranes. *Journal of Applied Mechanics*, **64**(2):257–262.

Lubowiecka, I., Szepietowska, K., Tomaszewska, A., Bielski, P. M., Chmielewski, M., Lichodziejewska-Niemierko, M., and Szymczak, C. (2022). A novel in vivo approach to assess strains of the human abdominal wall under known intraabdominal pressure. *Journal of the Mechanical Behavior of Biomedical Materials*, **125**:104902.

Lubowiecka, I., Tomaszewska, A., Szepietowska, K., Szymczak, C., Lichodziejewska-Niemierko, M., and Chmielewski, M. (2017). Membrane model of human abdominal wall. simulations vs. in vivo measurements. In *Shell Structures: Theory and Applications Volume 4*, volume **4**, pages 503–506. CRC Press.

Manh, N. D., Evgrafov, A., Gersborg, A. R., and Gravesen, J. (2011). Isogeometric shape optimization of vibrating membranes. *Computer Methods in Applied Mechanics and Engineering*, **200**(13-16):1343–1353.

Marek, A., Davis, F. M., and Pierron, F. (2017). Sensitivity-based virtual fields for the non-linear virtual fields method. *Computational Mechanics*, **60**(3):409–431.

Martins, J., Andrade-Campos, A., and Thuillier, S. (2018). Comparison of inverse identification strategies for constitutive mechanical models using full-field measurements. *International Journal of Mechanical Sciences*, **145**:330–345.

MATLAB (2018). *Version 9.5.0 (R2018b)*. The MathWorks Inc., Natick, Massachusetts.

Mei, Y. and Avril, S. (2019). On improving the accuracy of nonhomogeneous shear modulus identification in incompressible elasticity using the virtual fields method. *International Journal of Solids and Structures*, **178**:136–144.

Moulton, M. J., Creswell, L. L., Actis, R. L., Myers, K. W., Vannier, M. W., Szabo, B. A., and Pasque, M. K. (1995). An inverse approach to determining myocardial material properties. *Journal of Biomechanics*, **28**(8):935–948.

Nguyen, V. P., Anitescu, C., Bordas, S. P., and Rabczuk, T. (2015). Isogeometric analysis: an overview and computer implementation aspects. *Mathematics and Computers in Simulation*, **117**:89–116.

Nguyen-Thanh, N., Kiendl, J., Nguyen-Xuan, H., Wüchner, R., Bletzinger, K., Bazilevs, Y., and Rabczuk, T. (2011). Rotation free isogeometric thin shell analysis using PHT-splines. *Computer Methods in Applied Mechanics and Engineering*, **200**(47-48):3410–3424.

Oberai, A. A., Gokhale, N. H., and Feijóo, G. R. (2003). Solution of inverse problems in elasticity imaging using the adjoint method. *Inverse Problems*, **19**(2):297.

Pachera, P., Pavan, P., Todros, S., Cavinato, C., Fontanella, C., and Natali, A. (2016). A numerical investigation of the healthy abdominal wall structures. *Journal of Biomechanics*, **49**(9):1818–1823.

Pierron, F., Avril, S., and Tran, V. T. (2010). Extension of the virtual fields method to elasto-plastic material identification with cyclic loads and kinematic hardening. *International Journal of Solids and Structures*, **47**(22-23):2993–3010.

Pierron, F. and Grédiac, M. (2012). *The Virtual Fields Method: Extracting Constitutive Mechanical Parameters from Full-field Deformation Measurements.* Springer Science & Business Media.

Pierron, F. and Grédiac, M. (2021). Towards material testing 2.0. A review of test design for identification of constitutive parameters from full-field measurements. *Strain*, **57**(1):e12370.

Raghavan, M. and Vorp, D. A. (2000). Toward a biomechanical tool to evaluate rupture potential of abdominal aortic aneurysm: identification of a finite strain constitutive model and evaluation of its applicability. *Journal of Biomechanics*, **33**(4):475–482.

Roohbakhshan, F., Duong, T. X., and Sauer, R. A. (2016). A projection method to extract biological membrane models from 3D material models. *Journal of the Mechanical Behavior of Biomedical Materials*, **58**:90–104.

Roohbakhshan, F. and Sauer, R. A. (2017). Efficient isogeometric thin shell formulations for soft biological materials. *Biomechanics and Modeling in Mechanobiology*, **16**(5):1569–1597.

Sauer, R. A. (2018). On the computational modeling of lipid bilayers using thin-shell theory. In Steigmann, D., editor, *The Role of Mechanics in the Study of Lipid Bilayers*, pages 221–286. Springer.

Sauer, R. A. and Duong, T. X. (2017). On the theoretical foundations of thin solid and liquid shells. *Mathematics and Mechanics of Solids*, **22**(3):343–371.

Sauer, R. A., Duong, T. X., and Corbett, C. J. (2014). A computational formulation for constrained solid and liquid membranes considering isogeometric finite elements. *Computer Methods in Applied Mechanics and Engineering*, **271**:48–68.

Schillinger, D. (2018). Isogeometric finite element analysis. In Altenbach, H. and Öchsner, A., editors, *Encyclopedia of Continuum Mechanics*, pages 1–19. Springer.

Scott, M. A., Borden, M. J., Verhoosel, C. V., Sederberg, T. W., and Hughes, T. J. R. (2011). Isogeometric finite element data structures based on Bézier extraction of T-splines. *International Journal for Numerical Methods in Engineering*, **88**(2):126–156.

Seo, Y.-D., Kim, H.-J., and Youn, S.-K. (2010). Isogeometric topology optimization using trimmed spline surfaces. *Computer Methods in Applied Mechanics and Engineering*, **199**(49-52):3270–3296.

Seshaiyer, P. and Humphrey, J. D. (2003). A sub-domain inverse finite element characterization of hyperelastic membranes including soft tissues. *Journal of Biomechanical Engineering*, **125**(3):363–371.

Sigmund, O. and Petersson, J. (1998). Numerical instabilities in topology optimization: a survey on procedures dealing with checkerboards, mesh-dependencies and local minima. *Structural Optimization*, **16**(1):68–75.

Simón-Allué, R., Calvo, B., Oberai, A. A., and Barbone, P. (2017). Towards the mechanical characterization of abdominal wall by inverse analysis. *Journal of the Mechanical Behavior of Biomedical Materials*, **66**:127–137.

Song, C., Alijani, A., Frank, T., Hanna, G., and Cuschieri, A. (2006). Mechanical properties of the human abdominal wall measured in vivo during insufflation for laparoscopic surgery. *Surgical Endoscopy And Other Interventional Techniques*, **20**(6):987–990.

Steigmann, D. J. (2013). Koiter's shell theory from the perspective of three-dimensional nonlinear elasticity. *Journal of Elasticity*, **111**(1):91–107.

Strang, G. and Fix, G. (1973). *An Analysis of the Finite Element Method*. Series in Automatic Computation. Prentice-Hall.

Szymczak, C., Lubowiecka, I., Tomaszewska, A., and Śmietański, M. (2012). Investigation of abdomen surface deformation due to life excitation: implications for implant selection and orientation in laparoscopic ventral hernia repair. *Clinical Biomechanics*, **27**(2):105–110.

Tepole, A. B., Kabaria, H., Bletzinger, K.-U., and Kuhl, E. (2015). Isogeometric Kirchhoff–Love shell formulations for biological membranes. *Computer Methods in Applied Mechanics and Engineering*, **293**:328–347.

Vossen, Y. M. (1994). A mixed numerical experimental characterization of skin. Master's thesis, Eindhoven University of Technology.

Vu-Bac, N., Duong, T. X., Lahmer, T., Areias, P., Sauer, R. A., Park, H., and Rabczuk, T. (2019). A NURBS-based inverse analysis of thermal expansion induced morphing of thin shells. *Computer Methods in Applied Mechanics and Engineering*, **350**:480–510.

Vu-Bac, N., Duong, T. X., Lahmer, T., Zhuang, X., Sauer, R. A., Park, H., and Rabczuk, T. (2018). A NURBS-based inverse analysis for reconstruction of nonlinear deformations of thin shell structures. *Computer Methods in Applied Mechanics and Engineering*, **331**:427–455.

Wall, W. A., Frenzel, M. A., and Cyron, C. (2008). Isogeometric structural shape optimization. *Computer Methods in Applied Mechanics and Engineering*, **197**(33-40):2976–2988.

Wang, Y., Wang, Z., Xia, Z., and Poh, L. H. (2018). Structural design optimization using isogeometric analysis: a comprehensive review. *Computer Modeling in Engineering & Sciences*, **117**(3):455–507.

Wineman, A., Wilson, D., and Melvin, J. W. (1979). Material identification of soft tissue using membrane inflation. *Journal of Biomechanics*, **12**(11):841–850.

Wirgin, A. (2004). The inverse crime. `arXiv:math-ph/0401050`.

Wittek, A., Karatolios, K., Bihari, P., Schmitz-Rixen, T., Moosdorf, R., Vogt, S., and Blase, C. (2013). In vivo determination of elastic properties of the human aorta based on 4d ultrasound data. *Journal of the Mechanical Behavior of Biomedical Materials*, **27**:167–183.

Yuan, Y. (2000). A review of trust region algorithms for optimization. In *ICIAM*, volume **99**, pages 271–282.

Zhao, X. (2009). *Pointwise identification of elastic properties in nonlinear heterogeneous membranes, and application to soft tissues*. PhD thesis, The University of Iowa.

Zhao, X., Raghavan, M. L., and Lu, J. (2011). Identifying heterogeneous anisotropic properties in cerebral aneurysms: A pointwise approach. *Biomechanics and Modeling in Mechanobiology*, **10**(2):177–189.